

Mice Lacking Phosphatidylinositol Transfer Protein- α Exhibit Spinocerebellar Degeneration, Intestinal and Hepatic Steatosis, and Hypoglycemia*

Received for publication, April 7, 2003, and in revised form, May 30, 2003
Published, JBC Papers in Press, June 4, 2003, DOI 10.1074/jbc.M303591200

James G. Alb, Jr.[‡], Jorge D. Cortese[‡], Scott E. Phillips[‡], Roger L. Albin^{§¶}, Tim R. Nagy^{||},
Bruce A. Hamilton^{¶**}, and Vytas A. Bankaitis^{‡‡}

From the [‡]Department of Cell and Developmental Biology, Lineberger Comprehensive Cancer Center, University of North Carolina, Chapel Hill, North Carolina 27599-7090, the [§]Department of Neurology, University of Michigan School of Medicine, Ann Arbor Veterans Affairs Medical Center GRECC, Ann Arbor, Michigan 48104-0520, the ^{||}Department of Nutrition, University of Alabama at Birmingham, Birmingham, Alabama 35294, and ^{**}University of California School of Medicine, San Diego, La Jolla, California 92093-0644

Phosphatidylinositol transfer proteins (PITPs) regulate the interface between lipid metabolism and cellular functions. We now report that ablation of PITP α function leads to aponecrotic spinocerebellar disease, hypoglycemia, and intestinal and hepatic steatosis in mice. The data indicate that hypoglycemia is in part associated with reduced proglucagon gene expression and glycogenolysis that result from pancreatic islet cell defects. The intestinal and hepatic steatosis results from the intracellular accumulation of neutral lipid and free fatty acid mass in these organs and suggests defective trafficking of triglycerides and diacylglycerols from the endoplasmic reticulum. We propose that deranged intestinal and hepatic lipid metabolism and defective proglucagon gene expression contribute to hypoglycemia in PITP α ^{-/-} mice, and that hypoglycemia is a significant contributing factor in the onset of spinocerebellar disease. Taken together, the data suggest an unanticipated role for PITP α in with glucose homeostasis and in mammalian endoplasmic reticulum functions that interface with transport of specific luminal lipid cargoes.

PITPs¹ mobilize PtdIns or PtdCho between membrane bilayers *in vitro* (1, 2). *In vivo* studies demonstrate that PITPs control the interface between membrane trafficking and lipid metabolic pathways in yeast (3–6). By contrast, the physiological functions for mammalian PITPs, which are structurally unrelated to yeast PITPs (7, 8), are not understood at either the cellular or organismal levels.

Mammals express at least three soluble PITPs: PITP α ,

PITP β , and rdgB β (9–11). PITP α and PITP β share 77% primary sequence identity, are encoded by distinct genes, and exhibit biochemical differences. Yet both PITP α and PITP β (and even yeast PITPs) function as soluble factors that stimulate various reconstitutions of PIP-dependent functions in permeabilized mammalian cells. These functions include regulated and constitutive membrane trafficking and phospholipase C-dependent signaling through G-protein-coupled receptors (12–14). Given the lack of PITP specificity in these assays, it remains unclear how faithful such reconstitutions are in reporting physiological functions for mammalian PITPs.

Genetic studies are providing initial clues regarding PITP function in metazoans. An inherited form of light-enhanced retinal degeneration in *Drosophila* results from inactivation of a membrane-bound PITP (15). In mice, reduction of PITP α to 18% of wild-type levels is the basis for the *vibrator* neurodegenerative disorder (16, 26). Gene ablation approaches suggest PITP β plays an essential housekeeping function, whereas PITP α is nonessential for ES cell viability and is not a quantitatively significant factor in membrane trafficking, PIP metabolism, or growth factor signaling in ES cells (17).

In this report, we describe the consequences associated with ablation of PITP α function in the mouse. We find that PITP α , although dispensable for prenatal development, is required for neonatal survival. PITP α ^{-/-} neonates suffer from a severe spinocerebellar neurodegenerative disease and exhibit defects in dietary fat and α -tocopherol transport across the small intestine. This intestinal steatosis in some respects resembles CRD, a human disorder of unknown molecular etiology (18, 19). Liver steatosis is also prominent in the mutant mice, suggesting the possibility that PITP α nullizygosity also compromises lipoprotein assembly and/or neutral lipid secretion in hepatocytes. Finally, PITP α ^{-/-} mice are severely hypoglycemic. Our results suggest a novel and unanticipated role for PITP α in regulating cargo-specific lipid transport from the enterocyte and hepatocyte ER, endocrine pancreas function, and glycogen metabolism.

EXPERIMENTAL PROCEDURES

Generation and Genotyping of PITP α ^{-/-} Mice—AB1-derived +/PITP α :*neo** ES cells have been described previously (17). The +/PITP α :*neolpuro* ES cells corresponded to the OST 1152 line (Lexicon Genetics OmniBank™ library (20)). Mice were generated by injection of ES cells into C57BL/6 blastocysts, implantation of blastocysts into pseudopregnant foster mothers, and identification of male chimeric mice competent for germ line transmission of each allele. Genotypes for PITP α :*neo** mice (JG line) were determined by using a three-primer PCR assay. We employed a primer specific for the homozygous

* This work was supported in part by National Institutes of Health Grant NS37723 (to V. A. B.). The costs of publication of this article were defrayed in part by the payment of page charges. This article must therefore be hereby marked "advertisement" in accordance with 18 U.S.C. Section 1734 solely to indicate this fact.

¶ Recipient of a National Institutes of Health grant.

‡‡ To whom correspondence should be addressed. Tel.: 919-962-9870; Fax: 919-966-1856; E-mail: vytas@med.unc.edu.

¹ The abbreviations used are: PITPs, phosphatidylinositol transfer proteins; CHOP, CCAAT/enhancer-binding protein homology protein; CL, cardiolipin; CRD, chylomicron retention disease; DAG, diacylglycerol; ER, endoplasmic reticulum; ES cells, embryonic stem cells; FFA, free fatty acids; GFAP, glial fibrillary acidic protein; GM, gray matter; Glc-6-Pase, glucose-6-phosphatase; MEFs, murine embryonic fibroblasts; PIP, phosphoinositide; PtdCho, phosphatidylcholine; PtdIns, phosphatidylinositol; TG, triglyceride; TUNEL, terminal deoxynucleotidyltransferase-mediated dUTP nick-end-labeling; UPR, unfolded protein response; WM, white matter; CE, cholesteryl ester.

PITP $\alpha^{+/+}$ genotype (AB-2; 5'-GCGAGGCATCACTCTTCCCCTC-3'), the heterozygous *PITP* $\alpha^{-/+}$ genotype (AB-1B; 5'-CACCATCCCCACGGTGACTG-3'), and the *PITP* $\alpha^{-/-}$ genotype (PG-1; 5'-GAATGTGTGCGAGGCCAGAGG-3') in a 33-cycle reaction (53 °C annealing temperature). Genotypes for *PITP* $\alpha::neo/puro$ mice (L1 line) were determined in two steps. First, a two primer assay that monitored *Neo* distinguishes *PITP* $\alpha^{+/+}$ from *PITP* $\alpha^{-/+}$ and *PITP* $\alpha^{-/-}$ mice. Primers GE-UP (5'-GGGCGCCCGTTCCTTT TTGTGA-3') and GE-DO (5'-TTGGTGGTC-GAATGGGCAGGTAGC-3') were used in a 28-cycle reaction (60 °C annealing temperature). To distinguish *PITP* $\alpha^{-/+}$ from *PITP* $\alpha^{-/-}$ L1 mice, we resorted to immunoblot analyses of mouse brain using *PITP* α -specific serum (17).

Serum Analyses—Blood was collected from mice immediately after heart puncture and clotted, and serum was clarified by centrifugation. Serum glucose was determined by using either the Trinder assay (Sigma) or was measured by Antech Diagnostics (Farmingdale, NY). Insulin and β -hydroxybutyrate were determined using the Immunoassay System (Crystal Chem Inc.) and the β -hydroxybutyrate assay kit (Sigma), respectively. All other serum analyses were performed by Antech Diagnostics (Farmingdale, NY).

Carcass Analyses—Carcass analyses were as described previously (21). Gastrointestinal tracts were removed (stomach, small and large intestine, and cecum) and carcasses weighed. Body water content of eviscerated carcasses was determined by drying to constant weight in a 60 °C oven and measuring differences between the pre- and post-drying carcass mass. Dried carcasses were minced, ground to a homogeneous mixture, and extracted with petroleum ether in a Soxhlet apparatus to determine fat mass and fat-free dry mass. Fat-free dry mass was burned overnight at 600 °C (>8 h) to determine eviscerated carcass ash.

Histological Analysis—Mice were anesthetized with 1.25% Avertin and perfused with phosphate-buffered saline, 4% paraformaldehyde. Duodenum, ileum, cerebellum, pancreas, and spinal cord were harvested, flushed with fixative (duodenum and ileum only), dissected, and infused with fixative for 24 h. Samples were mounted in paraffin, and 5- μ m-thick sections were stained and mounted. These sections were rehydrated by serial transfer from xylene to 50% EtOH, stained with hematoxylin/eosin, and mounted in Permount (Fisher). Where osmium staining was employed, duodenal and liver sections were stained in 5% potassium dichromate, 2% osmium tetroxide for 8 h prior to paraffin embedding (22) and counterstained with toluidine blue O.

Whole brains were extracted from mice perfused with 4% paraformaldehyde and 2.5% glutaraldehyde, washed for several days in phosphate-buffered saline, and mounted in paraffin. Brains were sliced in half along the sagittal plane; each half was embedded in paraffin; and 5- or 8- μ m-thick slices were mounted onto treated slides. Sections were rehydrated to 50% EtOH. For visualization of Purkinje cells, slices were incubated with goat anti-calbindin antibodies (Santa Cruz Biotechnology; Santa Cruz, CA) and developed with the Vectastain ABC kit (Vector Laboratories, Burlingame, CA). After incubation in 2% osmium fumes for 10 min, slices were counterstained with toluidine blue O.

For Oil Red O staining, livers were extracted from mice perfused with 4% paraformaldehyde, washed with phosphate-buffered saline, and frozen at -20 °C. Frozen livers were mounted, sectioned (8 μ m), fixed to a histological slide, and placed in absolute propylene glycol (2 min). Slides were moved into Oil Red O solution (Newcomer Supply, Middleton, WI, catalog number 12722) for 1 h, differentiated in 85% propylene glycol (1 min), rinsed 2 \times in distilled water, counterstained with hematoxylin (10 s), and mounted in glycerin.

Electron Microscopy—Mice were perfused with 4% formaldehyde, 2.5% glutaraldehyde. Biopsies from intestine, liver, and spinal cord were post-fixed with 1% OsO₄, dehydrated with acetone, embedded in epoxy (23), sectioned (65 nm-thick), and stained with 4% uranyl acetate and Sato's lead mixture (24). Samples were viewed at 80 kV in a Phillips Tecnai 12 microscope (FEI Co., Eindhoven, The Netherlands) and imaged with a Gatan MultiScan model 794 digital camera (Gatan, Pleasanton, CA).

Epoxy-embedded samples were sectioned for histological analysis (2- μ m thickness) and stained with 1% toluidine blue O in 1% sodium borate. Digital images were collected with a SPOT RT digital camera (Diagnostic Instruments, Inc., Sterling Heights, MI), using Plan Fluor Nikon objectives mounted in a Nikon Eclipse E400 microscope (Nikon Inc., Melville, NY). Morphometric analysis of spinal cord sections was carried out with Scion Image software (Scion Corp., Frederick, MD).

α -Tocopherol Analyses—Brain α -tocopherol was extracted as described (25), injected onto a 250 \times 4.6 mm Phenomenex ODS 20 reversed phase C18 column (5- μ m particle diameter), and eluted with methanolic 0.05% ammonium acetate using a flow rate of 1.5 ml/min. The high pressure liquid chromatography system consisted of a

PerkinElmer Life Sciences model LC200 gradient pump, an AS 200 Autosampler, and an LC 295 programmable UV-visible light detector set at 292 nm.

Liver Glycogen Analysis—Quantification of liver glycogen was by the method of Passonneau and Lauderdale (26). Glycogen was extracted from acidified liver homogenates and hydrolyzed to glucose with amyloglucosidase (Sigma). Glucose was determined by a glucose oxidase-coupled Trinder assay (Sigma).

Adenylate Nucleotide Analysis—ATP and ATP/ADP ratios were measured using the ApoGlow™ kit (BioWhittaker Molecular Applications; Rockville, MD). Samples (0.5 mg tissue) were collected and rapidly frozen. Tissues were thawed and homogenized in the presence of a nucleotide-releasing mixture supplied by the manufacturer. Acid-extracted ATP was assayed with a luciferase-based system with picomolar sensitivity. ADP was converted to ATP and measured after a 5-min incubation at 22 °C.

Pancreatic Histology—Whole pancreas from mice perfused with 4% paraformaldehyde was embedded in paraffin and serially sectioned (thickness = 5 μ m). Islet numbers were assessed by sequential observation of hematoxylin/eosin-stained sections. Care was exercised to separate islets from patches of connecting ducts and intervening connective tissue, and not to re-score the same islet in successive sections. Islet-like, encapsulated structures larger than 100 μ m that were detected in at least three consecutive sections were scored as islets. The total pancreatic area studied was similar in all sections.

RESULTS

***PITP* $\alpha^{-/-}$ Mice Develop to Term**—Ablation of *PITP* α function in the mouse was achieved using two independent null alleles. First, a homologous recombination vector was constructed where exons 8–10 of the *PITP* α gene are replaced with a *neo* cassette (Fig. 1A). This mutation (*PITP* $\alpha\Delta::neo^*) deletes *PITP* α residues 162–257, a region critical for *PITP* α function (17). Second, survey of the Lexicon Genetics OmniBank™ gene trap library (see “Experimental Procedures”) identified an insertion mutation in the *PITP* α structural gene (*PITP* $\alpha::neopuro). This allele is genetically similar (although not identical) to *PITP* $\alpha\Delta::neo^* as it also truncates *PITP* α after residue 162 (Fig. 1B). Mice were derived from each targeted ES cell line. *PITP* $\alpha^{-/+}$ offspring are phenotypically normal and fertile, and mice homozygous for either of these two mutations exhibit indistinguishable phenotypes. The phenotypic data presented below were obtained from both *PITP* $\alpha\Delta::neo^* and *PITP* $\alpha::neopuro$ homozygous animals.$$$$

Intercrosses with heterozygous mice carrying either *PITP* $\alpha\Delta::neo^* or the *PITP* $\alpha::neopuro$ allele yielded genotypes consistent with a fully penetrant autosomal recessive mutation. From a dedicated pool of 408 live births, 89 *PITP* $\alpha^{-/-}$ progeny were recovered (Fig. 1C). The genotypic distribution of 106 *PITP* $\alpha^{+/+}$, 213 *PITP* $\alpha^{-/+}$, 89 *PITP* $\alpha^{-/-}$ corresponds to a 1.000:2.009:0.840 ratio that approximates closely the 1:2:1 ratio predicted by Mendel's rules. Correct gene targeting in the progeny was verified by PCR genotyping and immunoblotting of brain extracts with a specific *PITP* α antiserum (Fig. 1D). Antibodies directed against the *PITP* α N terminus failed to detect a truncation product in mice homozygous for *PITP* $\alpha\Delta::neo^* or *PITP* $\alpha::neopuro$, suggesting that both alleles represent null mutations. Finally, we find that relative *PITP* β levels are unchanged in *PITP* $\alpha^{+/+}$ and *PITP* $\alpha^{-/-}$ brain (Fig. 1D), indicating that *PITP* $\alpha^{-/-}$ mice do not activate compensatory processes that increase *PITP* β expression.$$

Neonatal Mortality of *PITP* $\alpha^{-/-}$ Mice—*PITP* $\alpha^{-/-}$ mice failed to thrive and died at a very young age. In a sample pool of 57 *PITP* $\alpha^{-/-}$ mice, 40% died within 48 h after birth (Fig. 2A). These early P0 and P1 deaths were not characterized by obvious external abnormalities. Moreover, postmortem analyses revealed that the stomachs of the expired *PITP* $\alpha^{-/-}$ mice contained copious quantities of milk, indicating that mutant animals had nursed. Of the *PITP* $\alpha^{-/-}$ progeny that survived past P1, a steady incidence of mortality was observed between

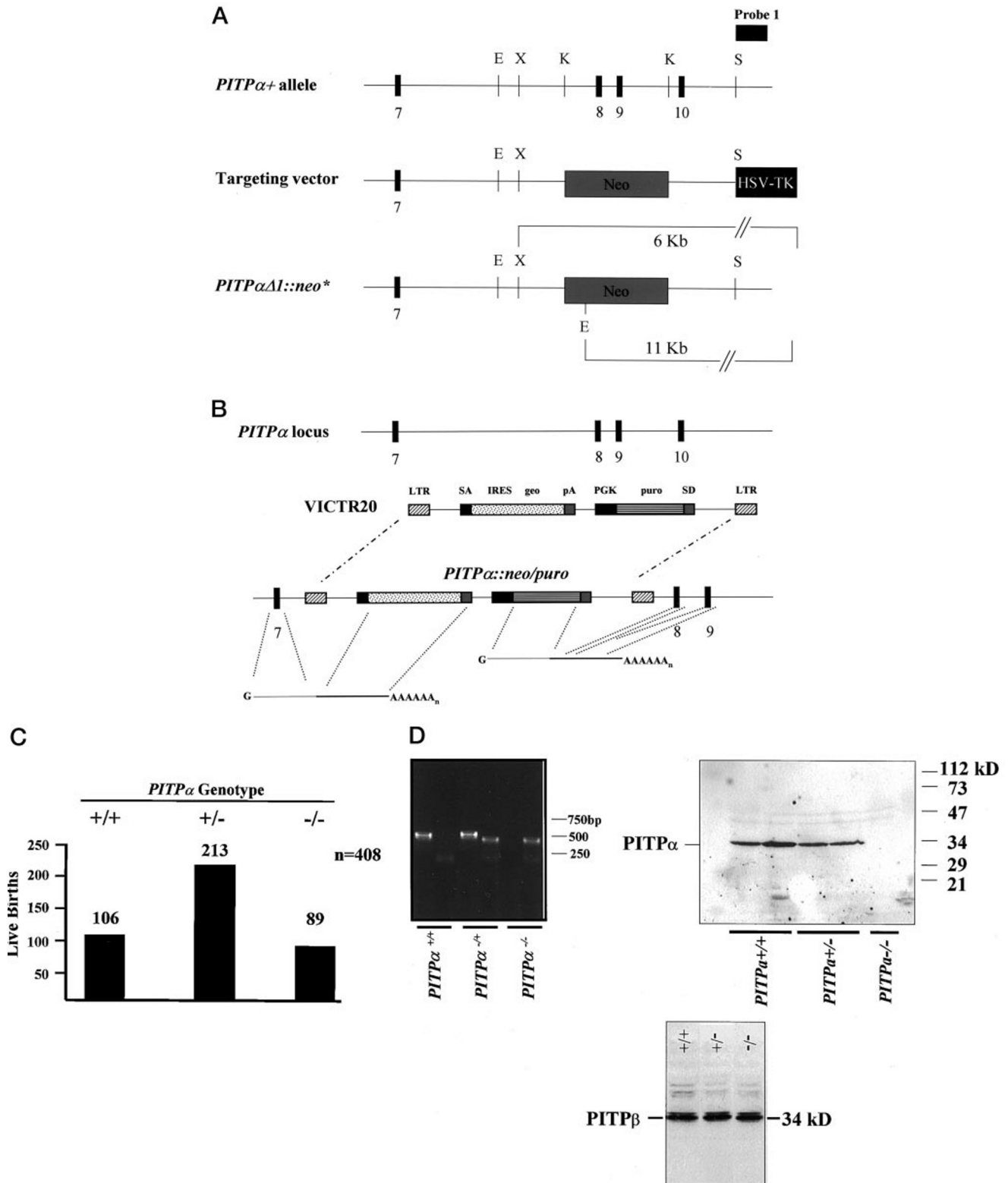


FIG. 1. Generation and characterization of PITP α -deficient mice. *A*, targeted replacement of the wild-type PITP α locus with PITP α Δ I::neo*. Organization of the targeting vector is shown. Probe 1 represents a 500-bp DNA fragment that resides outside the bounds of the targeting vector and is employed for diagnosis of targeting events. Exons 7–10 of the PITP α structural gene are indicated as closed bars and are numbered accordingly. Restriction enzyme sites: E, EcoRI; X, XbaI; K, KpnI; S, SacI. *B*, OmniBank™ gene trap library at the PITP α locus. Retroviral construct VICTR20 is depicted (20). The PITP α ::neo/puro mutation represents integration of VICTR20 between PITP α exons 7 and 8 and truncates PITP α after residue 162. The abbreviations used are as follows: LTR, long terminal repeat; PGK, phosphoglycerate kinase-1 promoter; puro, puromycin *N*-acetyltransferase gene; SD, splice donor sequence; SA, splice acceptor sequence; IRES, internal ribosome entry site; geo, galactosidase/neomycin phosphotransferase fusion gene; pA, polyadenylation sequence. *C*, distribution of PITP α genotypes in the F1. The number of live births obtained for each PITP α genotype (indicated at top), from a dedicated set of 408 F1 progeny of PITP α ^{+/+} intercrosses, is given above the corresponding bar. *D*, confirmation of viable PITP α ^{-/-} progeny. Upper left panel, diagnostic PCR profiles of PITP α ^{+/+}, PITP α ^{+/-}, and PITP α ^{-/-} progeny derived from a PITP α ^{+/-} intercross. Upper right panel, total brain lysates (20 μ g) harvested from each of five sibling pups (genotypes indicated) derived from a PITP α ^{+/-} intercross were resolved by SDS-PAGE and developed by immunoblotting with PITP α -specific antibodies. Lower panel, immunoblot of PITP β in brain lysates (20 μ g) from neonates of indicated genotype.

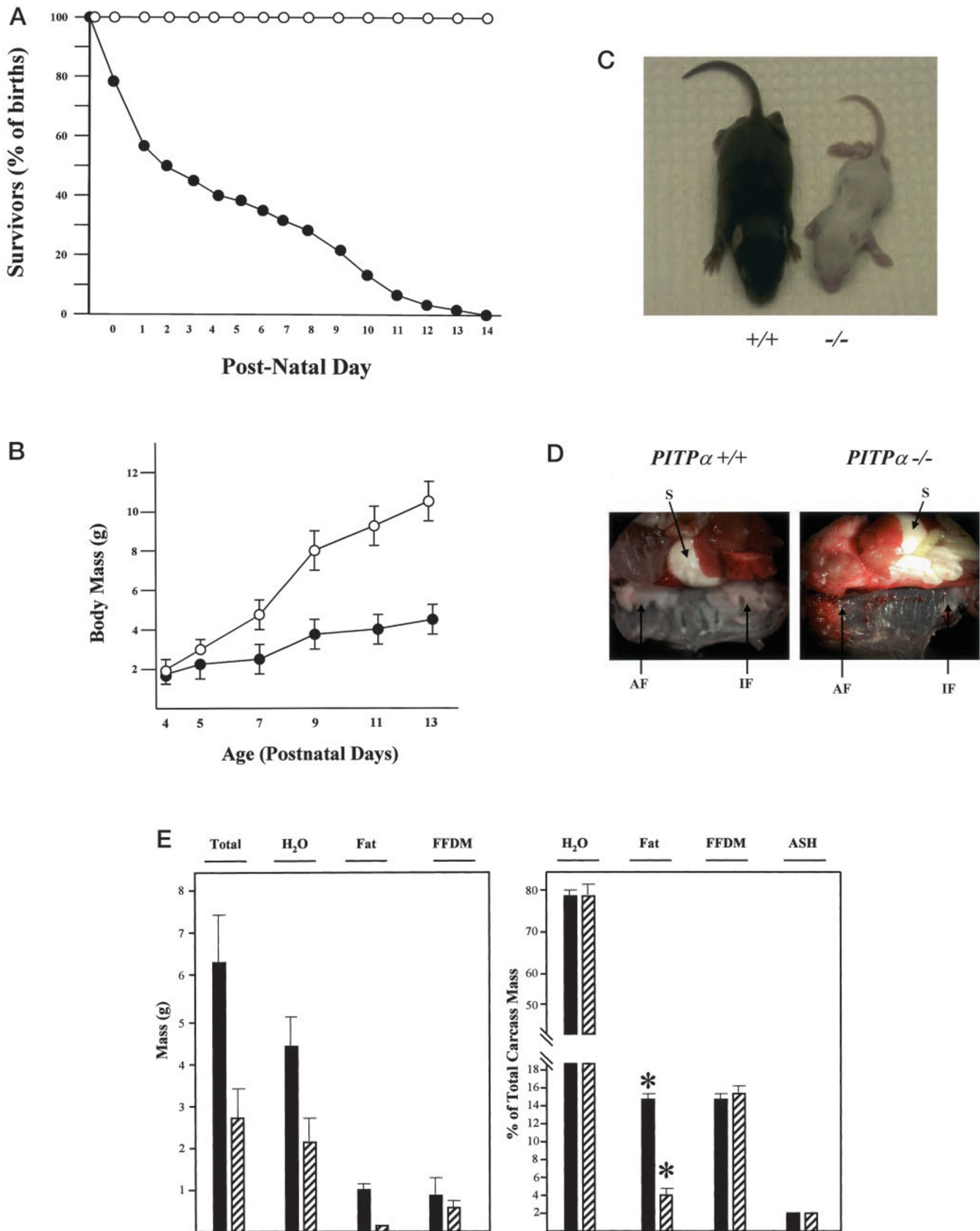


FIG. 2. Overt phenotypes of *PITP* $\alpha^{-/-}$ mice. *A*, mortality profile derived from a pool of 57 *PITP* $\alpha^{-/-}$ mice generated from 5 mating pairs over a period of 5 mating cycles. Data are presented as percentage of surviving progeny (+/+, open circles; -/-, closed circles) as a function of time (postnatal day). *B*, rates of body mass increase of *PITP* $\alpha^{+/+}$ and *PITP* $\alpha^{-/-}$ littermates. Values represent averages for two sibling mice of each genotype (+/+, open circles; -/-, closed circles). The data are representative. *C*, visual comparison of *PITP* $\alpha^{+/+}$ and *PITP* $\alpha^{-/-}$ littermates. Genotypes are at bottom. *D*, stomachs (*S*) of age-matched *PITP* $\alpha^{+/+}$ and *PITP* $\alpha^{-/-}$ mice (P7) are filled with milk. Subcutaneous axillary (*AF*) and inguinal (*IF*) fat pads are indicated. *E*, comprehensive chemical analysis of eviscerated carcasses. Measurements represent the averages from six P6 and three P8 *PITP* $\alpha^{+/+}$ animals (solid bars) and six P6 and three P8 *PITP* $\alpha^{-/-}$ mice (hatched bars). The abbreviations used are as follows: total, eviscerated carcass mass; *FFDM*, fat-free dry mass; and *ASH*, non-combustible carcass bone ash.

P2 and P11. Almost all mice expired by P11, and only one *PITPα*^{-/-} mouse lived to P14 (Fig. 2A).

PITPα^{-/-} progeny that survived past P1 were initially indistinguishable from *PITPα*^{+/+} and *PITPα*^{+/-} littermates in size, external morphology, and behavior. By P4, however, two phenotypes rapidly asserted themselves. First, most *PITPα*^{-/-} mice were moribund and exhibited little spontaneous movement. These mice did respond to touch, however. By contrast, ~10% of the *PITPα*^{-/-} mice experienced spontaneous seizures. All *PITPα*^{-/-} mice were severely ataxic and were generally incapable of maintaining themselves upright. We also observed coarse action tremors upon limb extension in *PITPα*^{-/-} mice. Second, these mutant mice failed to thrive. Although the *PITPα*^{-/-} mice gained body mass, they did so slowly (Fig. 2B). By P10, surviving *PITPα*^{-/-} mice were 2.5-fold less massive than their *PITPα*^{+/+} and *PITPα*^{+/-} littermates (Fig. 2C).

PITPα^{-/-} Mice Suckle Effectively—Several lines of evidence indicate that the failure of *PITPα*^{-/-} mice to thrive is not the simple consequence of neurological defects. We observed *PITPα*^{-/-} mice in the act of suckling, and postmortem analyses indicated both copious quantities of milk in stomachs of these mice (Fig. 2D) and substantial amounts of digested matter throughout the *PITPα*^{-/-} intestinal tract (not shown). The suckling competence of *PITPα*^{-/-} mice notwithstanding, the mutant animals exhibited pathologically low body fat levels. This reduction is obvious when the subcutaneous fat pads of *PITPα*^{+/+} and *PITPα*^{-/-} mice are compared. Whereas *PITPα*^{+/+} controls exhibit large axillary and inguinal fat pads, these structures are absent from *PITPα*^{-/-} animals (Fig. 2D). Chemical analyses of eviscerated carcasses quantified these differences; *PITPα*^{+/+} and *PITPα*^{-/-} mice exhibited total body fat contents of 15.0 ± 1.1 and 4.0 ± 0.5% of total body mass, respectively (Fig. 2E). Significantly, the relative water contents of *PITPα*^{+/+} and *PITPα*^{-/-} carcasses are similar (Fig. 2E), indicating that *PITPα*^{-/-} mice are not dehydrated, as would be expected if there were substantial suckling defects. The relative fat-free dry mass contents and carcass bone ash contents are also comparable (Fig. 2E). Consistent with those measurements, we find that organ/total body mass ratios in *PITPα*^{-/-} mice for brain, liver, and other major organs are also proportional to total body mass (not shown).

Elevated Apoptosis and Purkinje Cell Defects in PITPα^{-/-} Cerebellum—Nissl staining does not reveal obvious defects in development or morphology of *PITPα*^{-/-} cerebrum, thalamus, hippocampus, or cerebellum. Normal cellularity was observed in all regions examined (data not shown). However, *PITPα* insufficiencies evoked functional defects in the cerebellum. These defects were apparent at several levels. Whereas TUNEL staining showed a sparse and random distribution of apoptotic foci in wild-type brain, apoptosis was more prevalent throughout *PITPα*^{-/-} cerebellum. This is particularly evident in the external granule layer of mutant cerebellum (Fig. 3A).

Second, we find Purkinje cell defects in *PITPα*^{-/-} animals. Purkinje cells normally align themselves into a sharply defined monolayer that lies between the molecular and external granular layers of the cerebellum (Fig. 3B). These cells elaborate well developed apical dendritic stalks which arborize into luxuriant branches that penetrate into the molecular layer of the cerebellum. *PITPα*^{-/-} Purkinje cells, while retaining normal flask-shaped cell body morphologies, exhibit either abbreviated apical dendritic stalks or no obvious stalks at all (Fig. 3B). Moreover, the dendritic branches emanating from the abbreviated apical stalks are less arborized than those of *PITPα*^{+/+} Purkinje cells. We also observed cases where these cells exhibit defects in spatial alignment, reside off of the defined layer, or are otherwise misoriented.

Degenerative Disease in PITPα^{-/-} Cerebellum—*PITPα*^{-/-} cerebellum suffered major degenerative insult as judged by the extent of reactive gliosis. Wild-type cerebellum shows low levels of GFAP, a specific marker for activated astrocytes (Fig. 3C). By contrast, *PITPα*^{-/-} cerebellum exhibits a dramatic staining for GFAP, and reactive gliosis is especially prominent in the white matter trunk of this organ (Fig. 3C). Even in these relatively less affected areas, GFAP immunohistochemistry suggests some 10% of the cells represent activated astrocytes that are frequently seen to be enveloping neuron cell bodies (Fig. 3D). Reactive gliosis is not observed throughout the mutant brain. Whereas *PITPα*^{-/-} cerebellum and brain stem are heavily infiltrated with activated glial cells, and the subthalamic region is also involved, significant gliosis is not observed in the neocortex, striatum, hippocampal formation, and other forebrain regions (not shown).

Finally, electron microscopy reveals ER defects in cerebellar neurons of *PITPα*^{-/-} mice. These defects manifest themselves as significant vacuolations of the smooth ER region, even though adjacent regions of rough ER retain normal morphology (not shown). Such vacuolations are not observed in smooth ER of *PITPα*^{+/+} cerebellar neurons.

Neurodegeneration and Inflammation in PITPα^{-/-} Spinal Cord—We consistently observed WM deficits in *PITPα*^{-/-} cervical, thoracic, and lumbar spinal cord. Whereas ventral WM is well developed in *PITPα*^{+/+} cervical spinal cord, the corresponding WM regions are thin and sparse in *PITPα*^{-/-} animals (Fig. 4A). WM to GM area ratios in cervical spinal cord are 0.45 ± 0.1 for *PITPα*^{+/+} and 0.32 ± 0.02 for *PITPα*^{-/-} mice, respectively (*p* < 0.01; *n* = 6). In addition to the WM deficits, evidence of inflammation pervades all regions of the *PITPα*^{-/-} spinal cord. Toluidine blue O-staining reveals areas of abnormally heavy staining in the ventral horn where motor neuron cell bodies reside, suggesting cell damage in these areas (Fig. 4A). Moreover, whereas the WM/GM interface of *PITPα*^{+/+} cervical spinal cord presents normal vascular structures, neurons, and accessory cells, corresponding regions of the *PITPα*^{-/-} spinal cord exhibit densely stained cells and damaged neurons (Fig. 4B). These pathologies encompass a spectrum of cell death events. These range from occasional apoptotic neurons (condensed nuclei, fragmented cytoplasm; not shown) to large numbers of neurons undergoing apoptotic processes (Fig. 4B). Apoptosis is a form of cell death associated with reductions in cellular ATP and increases in ADP levels (27, 28). Analyses from six *PITPα*^{-/-} mice indicate that 18 ± 1% of the total motor neuron cell bodies in the ventral horn exhibit properties of apoptosis. These include pericytoplasmic vacuolation, reduced cytoplasmic contents, and cytoplasmic proliferation of irregular electron-translucent vesicles (Fig. 4B).

We did not observe apoptotic motor neurons in the ventral horn of *PITPα*^{+/+} spinal cord. Extensive vacuolation and membrane blebbing is prevalent in cells that line the vasculature of *PITPα*^{-/-} spinal cord (not shown). Axons surrounding capillaries and small vessels in the GM are enlarged and often damaged. This is unlikely to represent a perfusion artifact, as this phenotype was not recorded in any of the spinal cord sections analyzed from 14 *PITPα*^{+/+} mice.

Toluidine blue O-staining reveals the presence of cells containing an abundance of purple intracellular granules in the perivascular matrix (Fig. 4C, left panel). This obvious purple metachromasia is diagnostic of inflammatory mast cells (29, 30). Accordingly, we find extratissular macrophages in perivascular tissue or even in the vessels themselves (Fig. 4C, right panel), suggesting the blood/brain barrier of *PITPα*^{-/-} mice is itself compromised. Finally, spinocerebellar injury in *PITPα*^{-/-} mice also

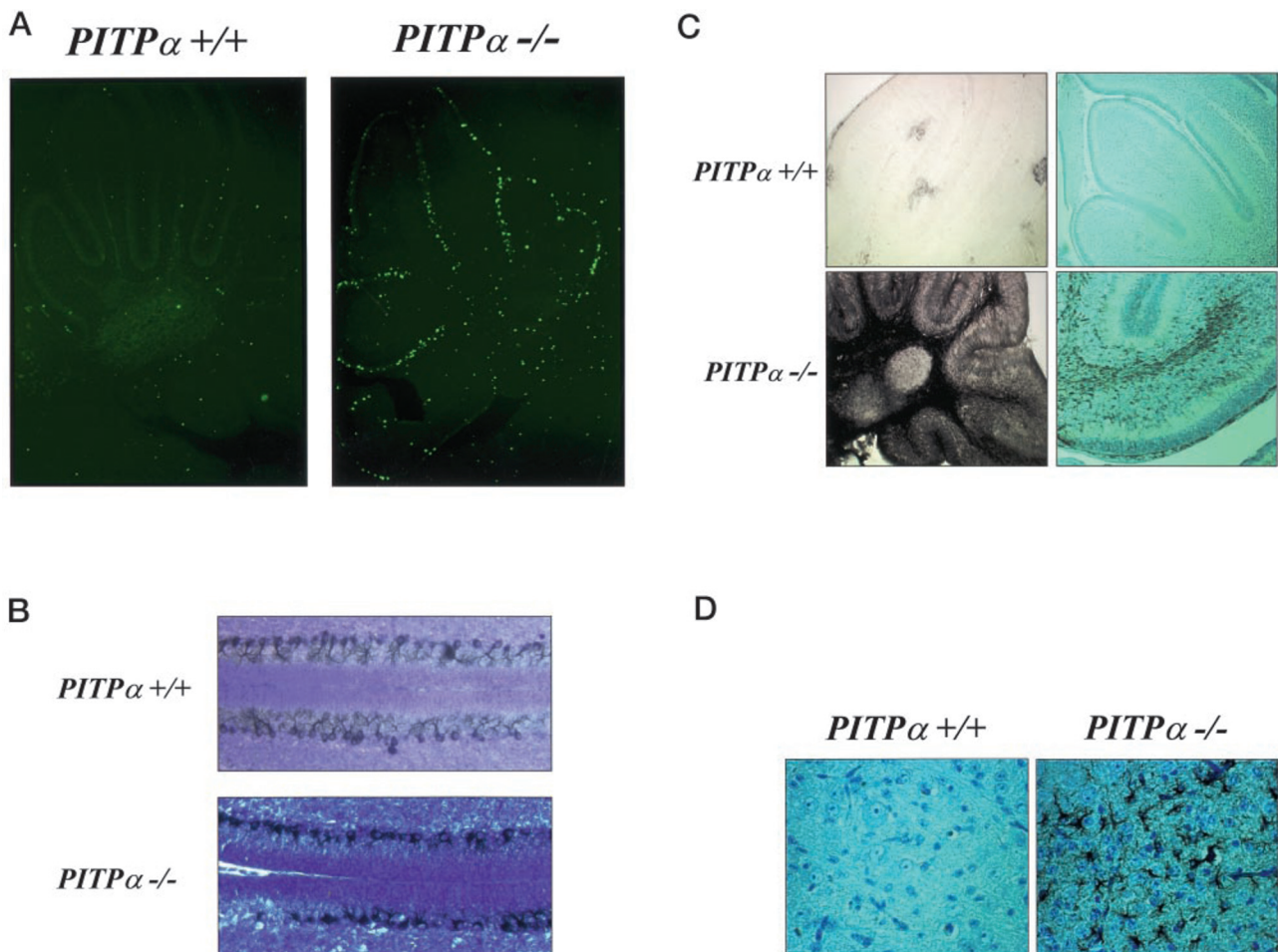


FIG. 3. **Cerebellar injury in *PITP* α -deficient mice.** A, TUNEL staining of cerebellum. Genotypes are indicated. The ApopTag Fluorescein *in Situ* Detection Kit (Intergen Co.) was used as instructed by the manufacturer. B, Purkinje cell defects in *PITP* α ^{-/-} cerebellum. The Purkinje cell layer was revealed by staining with calbindin antibodies and counterstaining with toluidine blue O. C, reactive gliosis in *PITP* α ^{-/-} cerebellum. Sagittal sections of *PITP* α ^{+/+} and *PITP* α ^{-/-} cerebellum (as indicated) were stained with anti-GFAP antibodies with or without counterstaining with toluidine blue O (right and left columns, respectively). D, higher magnification images of *PITP* α ^{+/+} and *PITP* α ^{-/-} cerebellum stained with anti-GFAP antibodies and counterstained with toluidine blue O. Genotypes are at top.

includes processes that resemble those of other myelin-related central nervous system inflammatory disorders (31). First, macroscopic swelling in the dorsal spinal columns is apparent. The non-neuronal area (neuropil) comprises $54 \pm 3\%$ in *PITP* α ^{+/+} spinal cord ($n = 6$; $p = 0.01$) and $70 \pm 6\%$ of total area in *PITP* α ^{-/-} spinal cord, respectively. Degenerative processes in neuropil, typified by swollen axons lacking organelles and cytoskeletal filaments, are also obvious (not shown). Second, demyelination is scored in both WM and GM areas of *PITP* α ^{-/-} mice and especially in the dorsal spinal columns. Supporting cells that may be remodeling myelin are also observed (Fig. 4D).

The fragility of the mutant central nervous system notwithstanding, a variety of *PITP* α ^{-/-} neurons are amenable to primary culture. Cultured cortical neurons, cerebellar granule cells, and spinal cord dorsal root ganglion neurons from *PITP* α ^{-/-} mice are not more fragile than their *PITP* α ^{+/+} counterparts in any obvious way. Indeed, titration of nerve growth factor concentrations from 50 to 5 ng/ml revealed no differences in the thresholds of trophic factor required to sustain viability of *PITP* α ^{-/-} versus *PITP* α ^{+/+} dorsal root ganglion neurons in culture (not shown). *PITP* α ^{-/-} cerebellar granule cells are similarly robust. These data suggest a significant cause of neuronal injury in *PITP* α ^{-/-} mice is a hostile physiological environment, rather than some overriding cell autonomous defect.

*Lipid Dysregulation in *PITP* α ^{-/-} Enterocytes*—Failure of

PITP α ^{-/-} mice to thrive suggests a malabsorption disorder. Histological analyses of duodenum indicate the architecture of this organ and its muscle layers are similar in *PITP* α ^{+/+} and *PITP* α ^{-/-} mice. Moreover, intestinal motility also appears normal (not shown). There are obvious anomalies in *PITP* α ^{-/-} intestinal epithelium, however. Most strikingly, *PITP* α ^{-/-} enterocytes exhibit an obviously heavy impregnation with the lipophilic agent osmium relative to *PITP* α ^{+/+} enterocytes (Fig. 5A). These histological properties are consistent with an abnormal accumulation of intracellular lipid in mutant enterocytes. If the accumulated lipid is derived from dietary fat, rather than manifestation of some other cellular pathology, active feeding is expected to be required for the loading of mutant enterocytes with lipid. Indeed, enterocytes harvested from *PITP* α ^{-/-} mice subjected to a 10-h fast are clear of accumulated lipid (not shown).

Closer inspection of *PITP* α ^{+/+} duodenal enterocytes by electron microscopy demonstrates that these cells contain a heterogeneous population of lipid bodies (Fig. 5B). Even at this high resolution, these structures stain with osmium in a manner consistent with a lipid interior, and these vesicles exhibit an average diameter of 300–700 nm. Inspection of the borders of these lipid bodies at very high magnifications reveals a classical trilaminar membrane surrounding these structures (not shown). *PITP* α ^{-/-} enterocytes, on the other hand, are packed with vesicles that are also membrane-enclosed but are much

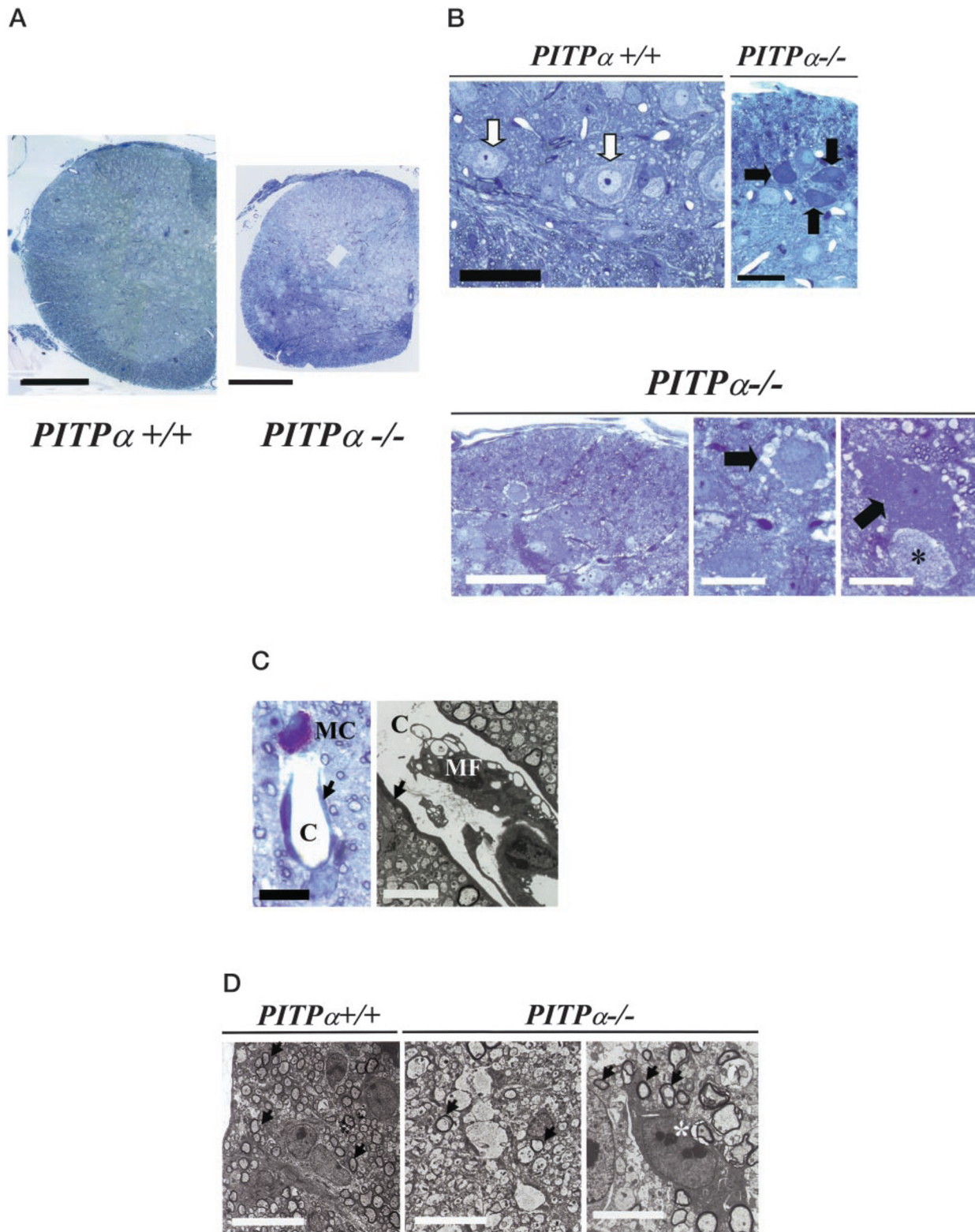


FIG. 4. Neurodegenerative and inflammatory changes in $PITP\alpha^{-/-}$ spinal cord. A, complete spinal cord sections were generated by reconstructing images from 2- μ m-thick, epoxy resin-embedded sections of $PITP\alpha^{+/+}$ stained with toluidine blue O (left, number of images $n = 30$) and $PITP\alpha^{-/-}$ spinal cord (right, $n = 22$). Bars are 0.15 mm. B, images from the ventral interface between gray and white matter (GM/WM interface) of cervical spinal cord sections. Top panels, representative images of $PITP\alpha^{+/+}$ motor neuron cell bodies (left, open arrows) and abnormally dark staining $PITP\alpha^{-/-}$ motor neuron cell bodies (right, dark arrows) are indicated. Bars are as follows: left, 50 μ m; right, 100 μ m. WM regions are indicated. Bottom panels, additional images from GM/WM interface of $PITP\alpha^{-/-}$ cervical spinal cord are shown. Characteristic neurodegenerative symptoms include highly vacuolated cells (center panel, solid arrow), dark cells (right panel, solid arrows), and abnormally lightly stained cells without discrete intracellular structure (right panel, *). Bars are as follows: left, 100 μ m; center, 50 μ m; right, 20 μ m. C, inflammatory cells in $PITP\alpha^{-/-}$ thoracic spinal cord. Left panel, mast cell (MC) and capillary lumen (C) are indicated. Right panel, macrophage (MF) and capillary lumen (C) are indicated. Bars are as follows: left, 20 μ m; right, 5 μ m. D, electron micrographs of myelin from the WM/GM interface of $PITP\alpha^{+/+}$ (left) and $PITP\alpha^{-/-}$ spinal cord (center). Examples of myelinated axons are indicated by arrows. Right panel, cells that may be remodeling myelin are present in large numbers in $PITP\alpha^{-/-}$ mice and an example is indicated (*). Bars are as follows: left, 15 μ m; center, 10 μ m; right, 6 μ m.

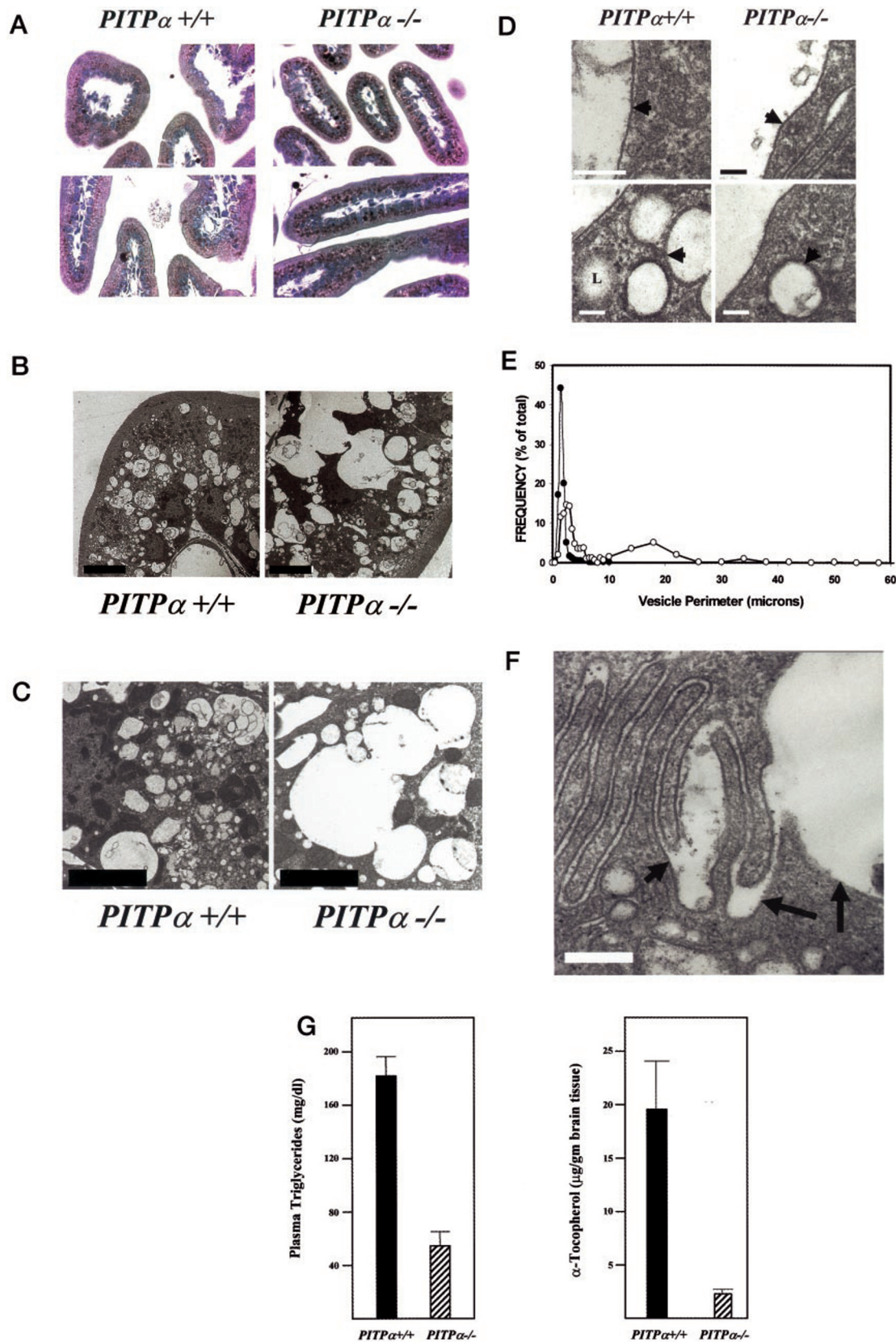


FIG. 5. Accumulation of lipid in *PITP* α ^{-/-} duodenal epithelium. A, intracellular lipid in enterocytes of *PITP* α ^{-/-} duodenum. Sections (5 μ m thick) of duodenum from *PITP* α ^{+/+} and *PITP* α ^{-/-} P5 siblings were stained with osmium and counterstained with toluidine blue O. Black granules identify lipid. Relevant genotypes are given. B, electron micrographs of duodenal epithelium from *PITP* α ^{+/+} (left) and *PITP* α ^{-/-} (right) P8 mice are shown. Bars are 5 μ m. C, electron micrographs of enterocytes from *PITP* α ^{+/+} and *PITP* α ^{-/-} mice as indicated. Bars are 2 μ m. D, electron micrographs of lipid bodies from *PITP* α ^{+/+} (left panels) and *PITP* α ^{-/-} enterocytes (right panels) as indicated. Dimensions of the lipid bodies aside, the general morphologies of these structures exhibit many similarities in wild-type versus mutant enterocytes, and most are membrane-enclosed. Boundary membranes are indicated by arrows. A cytoplasmic lipid droplet (L) with a fuzzy border is shown for contrast. Bars are 0.2 μ m. E, distribution histogram of vesicle perimeters in *PITP* α ^{+/+} (solid symbols) and *PITP* α ^{-/-} mice (open symbols). Perimeter measurements were made for 428 and 398 lipid bodies from *PITP* α ^{+/+} and *PITP* α ^{-/-} enterocytes, respectively. F, enlargement of smooth ER in *PITP* α ^{-/-}

larger than those observed in PITP $\alpha^{+/+}$ enterocytes. Moreover, the structures that accumulate in PITP $\alpha^{-/-}$ enterocytes often appear multilobed (Fig. 5C). Representative profiles of such structures from PITP $\alpha^{+/+}$ and PITP $\alpha^{-/-}$ enterocytes are shown at higher magnification in Fig. 5D. The size differences of the structures in wild-type and nullizygous enterocytes notwithstanding, these share many structural features. It is therefore likely that the biogenesis of the lipid bodies initially follows a common course in PITP $\alpha^{+/+}$ and PITP $\alpha^{-/-}$ enterocytes.

Morphometric measurements indicate a rather unimodal frequency distribution of vesicle perimeters from PITP $\alpha^{+/+}$ mice (average is $\sim 2 \mu\text{m}$; Fig. 5E). By contrast, the accumulated structures in PITP $\alpha^{-/-}$ enterocytes are much larger and have multimodal size distributions. Perimeters of $20 \mu\text{m}$ are often observed, and perimeters in excess of $50 \mu\text{m}$ are also encountered (Fig. 5E). Finally, our results indicate that the lipid structures in PITP $\alpha^{-/-}$ enterocytes reside predominantly in dilated regions of smooth ER (Fig. 5F).

α -Tocopherol and Plasma TG Deficiency in PITP $\alpha^{-/-}$ Mice—The failure of PITP $\alpha^{-/-}$ mice to thrive, when coupled with their retention of lipid in the enterocyte smooth ER, predicts a malabsorption-mediated deficit in fat-soluble vitamins, particularly α -tocopherol (vitamin E), and reduced levels of post-prandial plasma TGs. We find PITP $\alpha^{-/-}$ mice are deficient in α -tocopherol. Whereas PITP $\alpha^{+/+}$ brain exhibits $19.48 \pm 3.41 \mu\text{g}$ of α -tocopherol/gm tissue, values for PITP $\alpha^{-/-}$ brain are ~ 10 -fold reduced ($2.11 \pm 0.04 \mu\text{g}$ of α -tocopherol/g of tissue; Fig. 5G). Post-prandial plasma TG levels in PITP $\alpha^{-/-}$ mice are also ~ 3 -fold reduced relative to PITP $\alpha^{+/+}$ mice (55 ± 13 versus 183 ± 15 mg/dl).

By contrast, PITP $\alpha^{+/+}$ and PITP $\alpha^{-/-}$ plasma cholesterol levels are similar. Indeed, comprehensive blood chemistry analyses demonstrate many (although not all) parameters are largely normal for PITP $\alpha^{-/-}$ mice (Table I). Immunoblot experiments indicate that apolipoprotein B48 and microsomal triglyceride transfer protein, two components required for chylomicron assembly, are expressed in PITP $\alpha^{-/-}$ mice and that serum apoB levels are similar to those recorded for PITP $\alpha^{+/+}$ mice (not shown).

PITP $\alpha^{-/-}$ Mice Exhibit Microvesicular Steatosis in Liver—The pathways for lipid transport from the ER lumen to the cell surface are similar in enterocytes and hepatocytes. In that regard, PITP $\alpha^{-/-}$ liver also exhibits obvious microvesicular steatosis, as evidenced by its dramatically enhanced staining with osmium (Fig. 6A) and with the lipophilic dye Oil Red O (Fig. 6B). Because Oil Red O exhibits specific affinity for neutral lipids (e.g. TG, DAG, and CE), we conclude that the accumulated lipid is largely of the neutral class. These histochemical data are extended by electron microscopy. Relative to wild-type hepatocytes, PITP $\alpha^{-/-}$ cells exhibit an abundance of large intracellular lipid bodies. We often detect such structures in the nuclear matrix of mutant hepatocytes, a circumstance we have yet to encounter in wild-type cells (Fig. 6C).

The lipid bodies are either membrane-bound or represent large cytoplasmic lipid droplets (Fig. 6D). Unlike in mutant enterocytes, where accumulated lipid is predominantly found in membrane-enclosed compartments, $\sim 60\%$ of the lipid bodies in PITP $\alpha^{-/-}$ hepatocytes represent what we interpret to be cytosolic lipid droplets due to lack of identifiable boundary membrane (Fig. 6D). This raises the possibility that the mechanism of hepatic steatosis differs from that of the PITP $\alpha^{-/-}$

TABLE I
Serum analyses

Serum pooled from six PITP $\alpha^{+/+}$ and PITP $\alpha^{-/-}$ mice each, varying in age from P6 to P9, were subjected to a comprehensive mammalian chemistry panel performed by Antech Diagnostics (Farmingdale, NY). Values represent the averages of triplicate measurements obtained from three different sets of mice. Parameters that differ significantly between PITP $\alpha^{+/+}$ and PITP $\alpha^{-/-}$ mice are highlighted at top of the table. The abbreviations used are: APase, alkaline phosphatase; AST, aspartate aminotransferase; CPK, creatinine phosphokinase; ALT, alanine aminotransferase.

Parameter	PITP $\alpha^{+/+}$	PITP $\alpha^{-/-}$
Bilirubin	0.84 \pm 0.16 mg/dl	1.54 \pm 0.10 mg/dl
APase	809 \pm 160 units/liter	1497 \pm 179 units/liter
AST	135 \pm 9 units/liter	250 \pm 18 units/liter
CPK	4892 \pm 42 units/liter	6439 \pm 147 units/liter
Creatinine	0.44 \pm 0.08 mg/dl	0.44 \pm 0.08 mg/dl
Total protein	3.10 \pm 0.34 g/dl	3.10 \pm 1.33 g/dl
ALT	52.4 \pm 18.3 units/liter	46.1 \pm 13.2 units/liter
Albumin	1.70 \pm 0.18 g/dl	1.60 \pm 0.17 g/dl
Cholesterol	134 \pm 14 mg/dl	137 \pm 11 mg/dl
Calcium	7.04 \pm 0.24 mg/dl	8.28 \pm 1.70 mg/dl
Phosphorus	11.4 \pm 1.5 mg/dl	11.3 \pm 1.3 mg/dl
Sodium	115 \pm 14 Meq/liter	113 \pm 8 Meq/liter
Potassium	7.2 \pm 1.2 Meq/liter	7.3 \pm 0.9 Meq/liter
Chloride	50.6 \pm 11.9 Meq/liter	45.3 \pm 3.0 Meq/liter
Globulin	1.20 \pm 0.25 g/dl	1.50 \pm 32 g/dl
Urea N ₂	22.0 \pm 5.0 mg/dl	25.0 \pm 7.5 mg/dl

enterocytes. Although we cannot yet exclude the possibility that allocation of fatty acids and lipids between storage pools and lipoprotein pools is deranged in PITP $\alpha^{-/-}$ liver, at least some key fatty acid and lipid biosynthetic enzymes (acetyl-CoA carboxylase, stearyl-CoA reductase, and fatty-acid synthase) are not transcriptionally up-regulated in this mutant tissue (not shown). Moreover, the hepatic microvesicular steatosis, although qualitatively resistant to a short 6-h fast, is reversed by fasting mutant mice for 17 h (not shown).

Quantitative Analyses of Lipids and Fatty Acids in PITP $\alpha^{-/-}$ Liver and Brain—The lipid derangement in PITP $\alpha^{-/-}$ duodenum and liver suggests increased neutral lipid mass. To test this interpretation directly, the mass of a variety of lipid species in PITP $\alpha^{+/+}$ and PITP $\alpha^{-/-}$ liver and brain was quantified. The intestine provides technical challenges in this assay as the mice analyzed are neither fasted nor germ-free. We assume analysis of liver lipid mass is generally representative of the situation in intestine.

As shown in Fig. 7A, although the relative TG, DAG, and CE contents are very similar in matched wild-type and PITP α nullizygous brain tissue, bulk neutral lipid mass is dramatically elevated in PITP α nullizygous liver. Bulk TG and FFA mass is 2.0- and 2.6-fold increased relative to the respective values recorded for wild-type liver. Bulk CE and DAG mass is also increased in PITP $\alpha^{-/-}$ liver. Unexpectedly, PITP $\alpha^{-/-}$ brain exhibits a 3.3-fold increase in FFA mass relative to PITP $\alpha^{+/+}$ brain (Fig. 7A).

The derangements in neutral lipid/FFA content in PITP $\alpha^{-/-}$ tissues do not reflect a universal derangement of lipid homeostasis. PtdCho, phosphatidylethanolamine, and phosphatidylserine mass values are similar in matched wild-type and PITP α nullizygous brain and liver tissue (Fig. 7B). We do note, however, that mass of specific polar lipids such as sphingomyelin and lyso-PtdCho are elevated in PITP α nullizygous brain, and

duodenal enterocytes as revealed by electron microscopy. Lipid-engorged regions are identified by arrows. These smooth ER luminal regions are contiguous with the lumen of adjacent rough ER that is easily recognized by the associated ribosomes (not shown). Bar is $0.4 \mu\text{m}$. G, PITP $\alpha^{-/-}$ mice exhibit reduced brain α -tocopherol and post-prandial TG levels. Parameters are indicated. Measurements were made from nine PITP $\alpha^{+/+}$ and nine PITP $\alpha^{-/-}$ mice. Averages \pm S.D. are given.

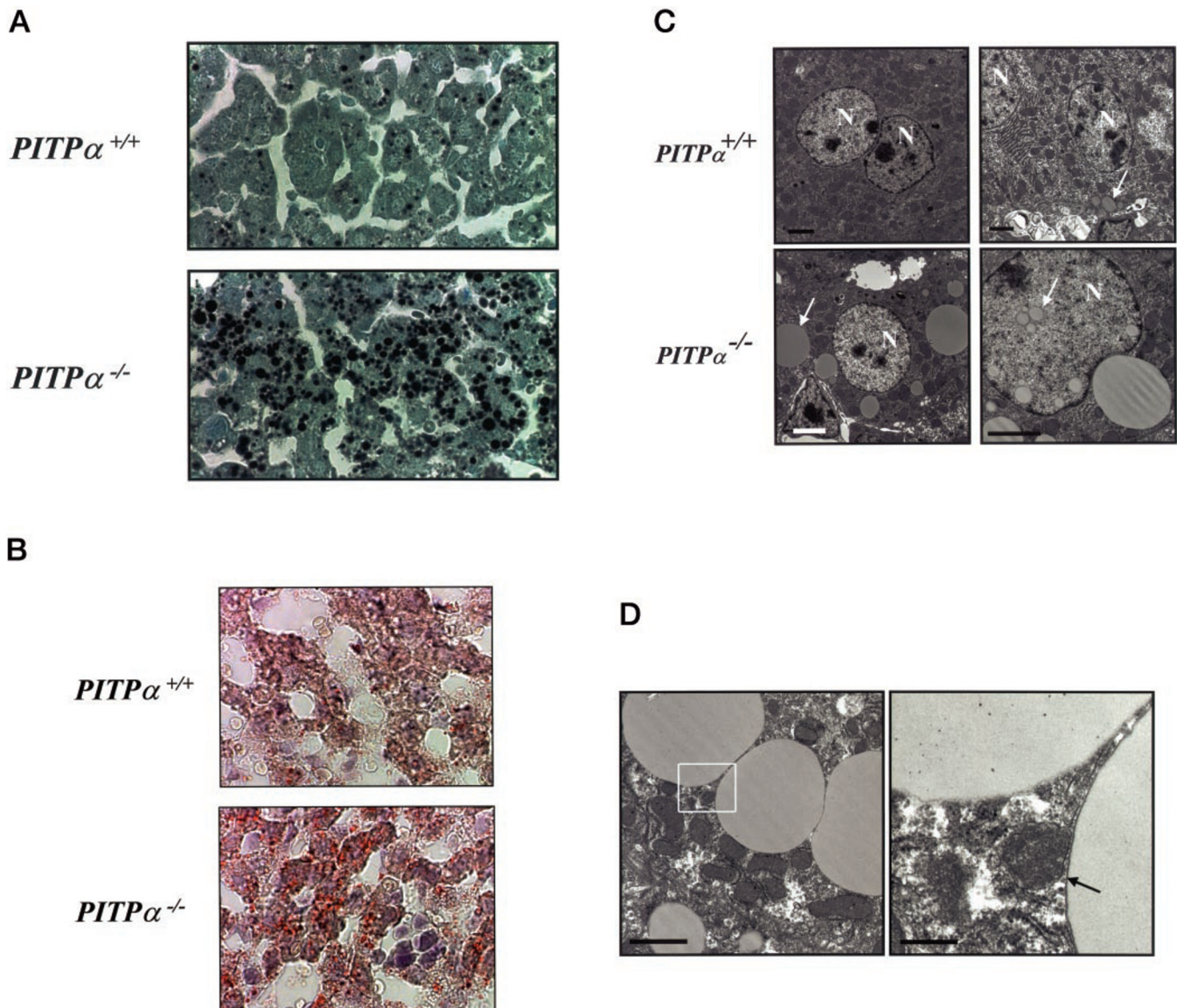


FIG. 6. Microvesicular steatosis in *PITP* $\alpha^{-/-}$ hepatocytes. *A*, liver sections from *PITP* $\alpha^{+/+}$ and *PITP* $\alpha^{-/-}$ P5 siblings were stained with osmium and counterstained with toluidine blue O. Black granules identify lipid. Relevant genotypes are given at left. *B*, liver sections from mice of the indicated genotype were stained with Oil Red O and counterstained with hematoxylin/eosin. The red globules prevalent in sections of *PITP* α nullizygous liver identify neutral lipid bodies. *C*, electron micrographs of *PITP* $\alpha^{+/+}$ and *PITP* $\alpha^{-/-}$ liver sections are shown. Nuclei (*N*) and examples of lipid bodies are highlighted by arrows. Bars (clockwise from upper left) are 2, 2, 3, and 2 μ m, respectively. *D*, electron micrograph of lipid bodies that accumulate in *PITP* α nullizygous hepatocytes. The right panel is a magnification of the region identified by the box in the left panel. One lipid body is membrane-enclosed (arrow), whereas the other lacks a distinct border and is interpreted to represent a large cytoplasmic lipid droplet. Bars (from left) are 2 and 0.4 μ m, respectively.

CL levels are altered in both mutant brain and liver relative to matched wild-type tissues (Fig. 7C).

Fatty acid compositions of the CE, DAG, TG, FFA, sphingomyelin, and CL pools of *PITP* $\alpha^{+/+}$ and *PITP* $\alpha^{-/-}$ brain (Table II) and liver (Table III) were also compared. The most striking qualitative and quantitative difference is the reduced content of 18:2n6 (9,12-octadecadienoic acid) in mutant brain TG, DAG, and CL pools (Table II), and an increase in 18:1n9 (9-octadenoic acid) in CE, DAG, and FFA pools in nullizygous liver (Table III). Fatty acid profiles of brain and liver lyso-PtdCho were determined for *PITP* $\alpha^{+/+}$ and *PITP* $\alpha^{-/-}$ mice, and no differences were scored (not shown).

Reduced ATP Content in *PITP* $\alpha^{-/-}$ Cerebellum and Liver—Electron microscopic analyses reveal not only lipid accumulation but also indications of aponecrosis in mutant hepatocytes. These indications resemble those observed in the *PITP* $\alpha^{-/-}$ spinocerebellar system (see above) and include the significantly

increased proliferation of electron-dense autophagic bodies throughout the cytoplasm (cytolysosomes) and regions of dilated smooth ER (not shown). Aponecrosis in the spinocerebellar system and in liver suggests a fundamental defect in energy metabolism in *PITP* α nullizygous mice. Indeed, ATP levels are diminished in *PITP* $\alpha^{-/-}$ relative to *PITP* $\alpha^{+/+}$ liver (40.4 ± 8.6 versus 98.1 ± 9.3 pmol of ATP/mg of tissue; Fig. 8A). ATP/ADP ratios further emphasize this reduction (2.8 ± 0.5 for *PITP* $\alpha^{-/-}$ and 9.1 ± 3.1 for *PITP* $\alpha^{+/+}$ liver; Fig. 8B). Similarly, *PITP* $\alpha^{+/+}$ and *PITP* $\alpha^{-/-}$ animals exhibit 83.3 ± 5.3 and 44.9 ± 5.9 pmol of ATP/mg of cerebellum, respectively (Fig. 8A). Reduced cerebellar ATP/ADP ratios are measured as well (7.7 ± 1.0 for wild-type versus 4.2 ± 0.5 for mutant; Fig. 8B). Interestingly, *PITP* $\alpha^{+/+}$ and *PITP* $\alpha^{-/-}$ brain ATP levels (40 ± 59 and 343 ± 65 pmol of ATP/mg of brain, respectively) and ATP/ADP ratios (13.6 ± 2.3 versus 9.1 ± 0.7 , respectively) are comparable, thereby regionally correlating neuronal and he-

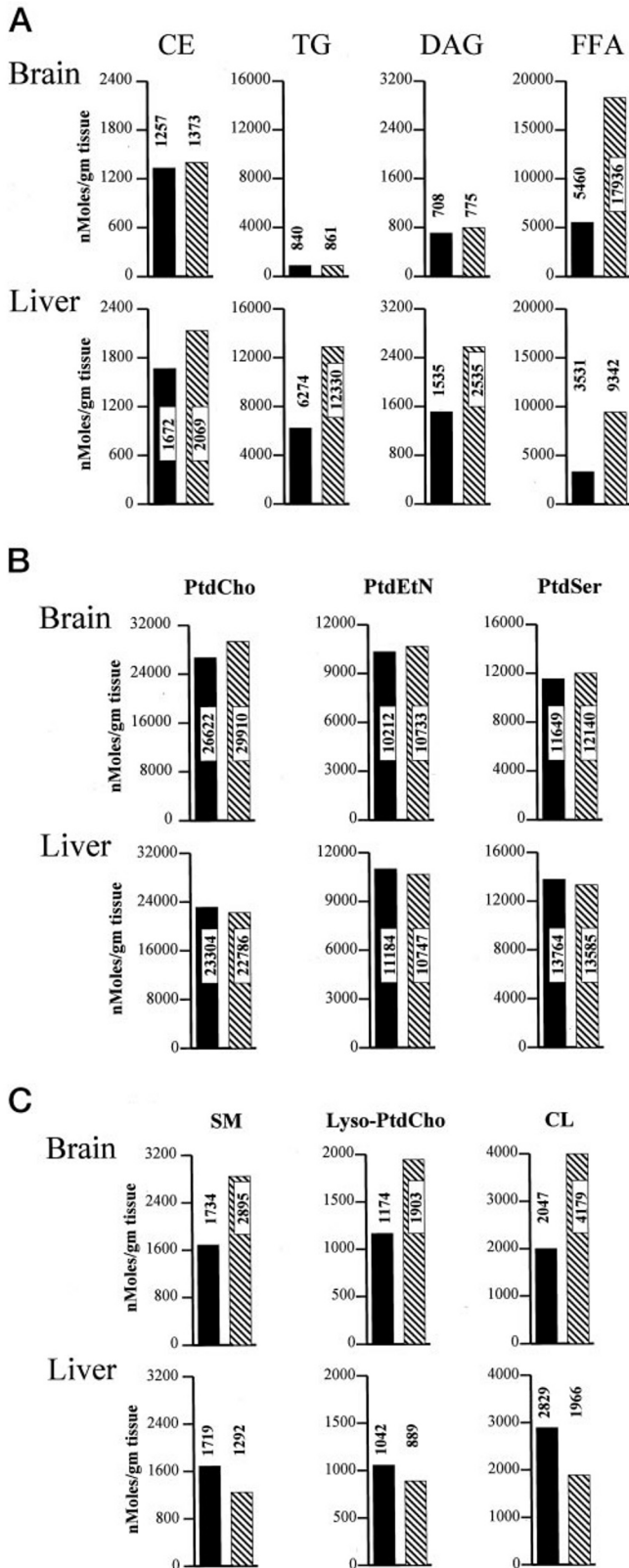


FIG. 7. Quantification of lipid mass in *PITP* $\alpha^{+/+}$ and *PITP* $\alpha^{-/-}$ brain and liver. Brains and livers were collected from each of four freshly euthanized non-fasted *PITP* $\alpha^{+/+}$ and *PITP* $\alpha^{-/-}$ mice and combined to generate defined tissue pools for each genotype. Pools were frozen and quantified for individual lipid species and FFAs via the Lipomics Technologies, Inc., TrueMassTM protocol. Individual lipid species are given at the top, and brain and liver values for each lipid species are given in a vertical column below each heading. Brain values are represented in the top panels, and the liver values are in the bottom panels as indicated. All lipid species are quantified as nanomoles per g of tissue. *PITP* $\alpha^{+/+}$ and *PITP* $\alpha^{-/-}$ values are indicated by solid bars

and hatched bars, respectively. Numerical values for each bar are given. *A*, neutral lipid mass measurements. *B*, polar lipids whose mass is unaltered in *PITP* $\alpha^{+/+}$ versus *PITP* $\alpha^{-/-}$ tissues. *C*, polar lipids whose mass is altered in *PITP* $\alpha^{+/+}$ versus *PITP* $\alpha^{-/-}$ tissues. *SM*, sphingomyelin; *PtdEtN*, phosphatidylethanolamine; *PtdSer*, phosphatidylserine.

patric injury with reduced cellular ATP (Fig. 8, *A* and *B*). The significant decrease in mass of the mitochondrial lipid CL in *PITP* $\alpha^{-/-}$ liver is consistent with energetic compromise (Fig. 7*C*). The mass increase of CL in *PITP* $\alpha^{-/-}$ brain may reflect compensatory attempts by this tissue to enhance mitochondrial activity in response to an unfavorable energy status (Fig. 7*C*).

Hypoglycemia in *PITP* $\alpha^{-/-}$ Mice—The aponecrotic cell death observed in the *PITP* $\alpha^{-/-}$ spinocerebellar system and liver diagnoses a systemic problem. In this regard, we find *PITP* $\alpha^{-/-}$ neonates are severely hypoglycemic. We measure 9-fold reductions in serum glucose levels of *PITP* $\alpha^{-/-}$ mice (9.6 ± 3.6 mg/dl) relative to *PITP* $\alpha^{+/+}$ siblings (88.0 ± 6.6 mg/dl serum; Fig. 9*A*). This reduction in serum glucose is of similar magnitude to that measured for *PITP* $\alpha^{+/+}$ mice that are fasted overnight, despite the fact that stomachs of all *PITP* $\alpha^{-/-}$ mice analyzed were filled with milk at the time of analysis (not shown).

Reduction in serum glucose is not secondary to hyperinsulinemia. Circulating insulin levels in *PITP* $\alpha^{-/-}$ mice are 9-fold lower than those of *PITP* $\alpha^{+/+}$ siblings (0.5 ± 0.2 versus 4.5 ± 0.2 ng/ml, respectively; Fig. 9*A*). Given the hypoglycemia of *PITP* $\alpha^{-/-}$ mice, these low insulin levels are appropriate (see below). We also measured an increase in circulating β -hydroxybutyrate in *PITP* $\alpha^{-/-}$ versus *PITP* $\alpha^{+/+}$ serum (19.1 ± 1.2 and 11.2 ± 1.8 mg/dl, respectively; Fig. 9*A*), and this increase is recapitulated in serum of *PITP* $\alpha^{+/+}$ mice that were fasted overnight (20.2 ± 0.1 mg/dl). β -Hydroxybutyrate is generated by mitochondrial oxidation of fatty acids and serves as an alternative energy source for hypoglycemic tissue. Modest elevations are scored for bilirubin and alkaline phosphatase in *PITP* $\alpha^{-/-}$ mice (consistent with modest hepatic stress), and a 2-fold increase in the gluconeogenic enzyme aspartate aminotransferase is also measured (Table I).

Reduced Proglucagon Gene Expression in *PITP* $\alpha^{-/-}$ Mice—Mice normally effect dramatic changes in circulating insulin, corticosteroid, and glucagon levels to activate hepatic gluconeogenesis late in gestation. This reprogramming of hormonal signaling serves as a protective mechanism for the impending loss of the glucose source provided by the maternal circulatory system *in utero* (33). Mutant animals are appropriately responding to hypoglycemia as evidenced by elevated levels of circulating corticosteroids, a hormonal stimulus for gluconeogenesis. Levels of plasma corticosteroid are highly elevated in *PITP* $\alpha^{-/-}$ mice relative to *PITP* $\alpha^{+/+}$ littermates (51.64 versus 19.58 ng/ml, respectively). We also compared expression of the gluconeogenic enzymes Glc-6-Pase and phosphoenolpyruvate carboxykinase in *PITP* $\alpha^{+/+}$ and *PITP* $\alpha^{-/-}$ mice. Expression of both genes in *PITP* $\alpha^{-/-}$ liver compares favorably to *PITP* $\alpha^{+/+}$ control as their corresponding mRNA levels in *PITP* $\alpha^{+/+}$ liver are 1.3 ± 0.1 - and 1.1 ± 0.2 -fold increased relative to those of *PITP* $\alpha^{-/-}$ liver (Fig. 9*B*). Thus, transcriptional control of key gluconeogenic enzymes also appears intact in the mutant mice. Elevated serum levels of the gluconeogenic enzyme aspartate aminotransferase in *PITP* $\alpha^{-/-}$ further support this conclusion (Table I).

By contrast, proglucagon gene expression is inappropriately depressed in *PITP* $\alpha^{-/-}$ animals (Fig. 9*B*). By using β -actin mRNA as a normalizing factor, proglucagon gene expression in pancreas is reduced 11.7 ± 0.1 -fold in *PITP* $\alpha^{-/-}$ mice relative to *PITP* $\alpha^{+/+}$ siblings. In independent agreement with the Northern data, we record a 5-fold reduction in circulating glu-

TABLE II
Acyl chain compositions of bulk brain lipids

Fatty acid compositions of the lipid classes analyzed from pooled brain tissue samples depicted in Fig. 7 were determined by Lipomics TrueMass™ technology. Profiles of the indicated fatty acid species (at left) for the indicated lipid species (at top) are presented in nanomoles of fatty acid/total moles of fatty acid in each lipid class. The data are presented as *PITP* $\alpha^{+/+}$ value/*PITP* $\alpha^{-/-}$ value. Some differences between corresponding *PITP* $\alpha^{+/+}$ and *PITP* $\alpha^{-/-}$ values are indicated in boldface. Omega fatty acid nomenclature is employed. The t prefix indicates trans-double bond, and the dm prefix indicates plasmalogen-linked fatty acid. SM indicates sphingomyelin. A precise molecular description of each fatty acid species analyzed is provided at www.lipomics.com/Fatty%20Acids/fatty_acid.htm.

Acyl species	CE	TG	DAG	FFA	SM	CL
14:0	5.4/6.0	3.3/0.0	4.1/5.4	4.1/4.2	2.6/3.5	1.9/2.0
14:1n5	0.0/0.0	0.7/1.0	0.0/0.0	0.0/0.0	0.1/0.2	0.0/0.0
15:0	1.0/1.6	1.6/2.8	0.8/1.1	1.3/1.0	0.5/1.1	1.2/1.7
dm16:0	1.7/3.3	0.7/1.3	0.0/0.4	0.0/0.3	0.2/0.3	2.6/3.1
16:0	23.2/21.4	27.2/28.5	28.9/36.0	33.4/33.9	17.1/16.8	16.1/16.9
t16:1n7	0.9/1.8	0.7/1.3	3.1/3.3	5.4/5.5	1.6/2.6	0.5/2.2
16:1n7	9.1/13.2	3.7/5.6	1.3/1.4	1.2/0.9	1.3/1.8	3.3/1.8
dm18:0	0.0/0.0	0.9/0.7	0.0/0.0	0.4/0.7	0.2/0.1	1.8/2.1
dm18:1n9	1.9/2.0	0.0/0.0	0.0/0.0	0.0/0.0	0.0/0.0	0.1/0.2
dm18:1n7	0.0/0.0	0.8/1.0	0.0/0.0	0.0/0.0	0.0/0.0	0.2/0.2
18:0	16.4/11.9	15.4/18.8	23.4/27.9	27.4/30.4	28.7/23.2	21.8/18.9
t18:1n9	0.0/0.0	0.0/0.0	0.0/0.4	0.0/0.0	0.3/0.9	0.0/0.0
18:1n9	12.3/11.5	17.3/18.2	15.2/8.7	12.2/10.7	18.4/25.0	6.0/6.0
18:1n7	0.6/0.0	1.5/1.2	1.6/1.0	1.5/1.3	1.7/1.7	2.1/1.5
t18:2n6	0.0/0.0	0.0/0.0	0.2/0.3	0.0/0.1	0.0/0.0	0.0/0.0
18:2n6	7.2/6.8	16.3/8.9	9.1/4.8	6.1/4.2	2.7/3.1	8.4/2.8
18:3n6	0.0/0.6	0.3/0.6	0.3/0.0	0.2/0.0	0.0/0.0	0.0/0.0
18:3n3	0.2/0.0	0.6/0.4	0.8/0.8	0.3/0.4	0.4/0.4	0.4/0.3
18:4n3	0.0/0.3	0.3/0.5	0.0/0.0	0.0/0.0	0.0/0.0	0.2/0.2
20:0	0.4/1.0	0.8/0.4	0.8/0.7	0.9/0.9	0.4/0.3	0.2/0.2
20:1n15	0.0/0.0	0.0/0.0	0.0/0.0	0.0/0.0	0.0/0.0	0.0/0.0
20:1n12	0.0/0.0	0.0/0.0	0.0/0.0	0.0/0.0	0.0/0.0	0.0/0.0
20:1n9	6.2/5.6	1.1/2.0	0.4/0.0	0.2/0.3	0.5/0.4	0.4/0.2
20:3n9	0.0/0.0	0.0/0.0	0.3/1.4	0.5/0.4	0.1/0.1	0.0/0.1
20:2n6	0.7/0.9	0.8/0.3	0.3/0.5	0.4/0.4	0.1/0.2	16.9/25.2
20:3n6	0.0/0.0	1.0/0.3	0.4/0.0	0.4/0.3	0.6/0.5	0.5/0.4
20:4n6	1.1/0.0	1.4/0.4	7.7/2.8	3.5/1.9	4.5/3.3	4.4/4.1
20:3n3	0.0/0.0	0.0/0.0	0.0/0.0	0.0/0.0	0.0/0.1	0.1/0.0
20:4n3	0.0/0.0	0.3/0.2	0.0/0.0	0.0/0.0	0.0/0.0	0.3/0.3
20:5n3	0.0/0.0	0.3/0.0	0.2/0.0	0.0/0.1	0.0/0.0	0.0/0.1
22:0	1.1/1.8	0.3/0.3	0.0/0.0	0.0/1.1	0.6/0.4	0.1/0.2
22:1n9	9.3/8.6	1.3/0.3	0.0/1.1	0.0/0.4	0.4/0.3	0.3/0.4
22:2n6	0.0/0.3	0.0/0.0	0.0/2.1	0.0/0.2	0.0/0.1	0.7/0.6
22:4n6	0.0/0.0	0.0/0.0	0.0/0.0	0.0/0.0	0.2/0.2	0.4/0.0
22:5n6	0.0/0.0	0.0/0.0	0.0/0.0	0.0/0.0	0.0/0.0	0.0/0.0
22:5n3	0.0/0.0	0.0/0.0	0.0/0.0	0.0/0.0	0.6/0.4	0.1/0.2
22:6n3	0.0/0.0	0.3/0.3	1.1/0.0	0.0/0.0	15.9/12.4	8.5/7.3
24:0	1.3/1.5	0.8/0.3	0.0/0.0	0.5/0.6	0.2/0.3	0.2/0.4
24:1n9	0.0/0.0	0.0/0.0	0.0/0.0	0.0/0.0	0.2/0.4	0.2/0.3
24:6n3	0.0/0.0	0.2/0.0	0.0/0.0	0.0/0.0	0.0/0.0	0.0/0.0

cagon levels in mutant animals (246.68 and 49.32 pg of glucagon/ml of plasma for *PITP* $\alpha^{+/+}$ and *PITP* $\alpha^{-/-}$ mice, respectively).

Glycogen Metabolism in *PITP* $\alpha^{-/-}$ Mice—Normally, liver glycogen is rapidly consumed in response to hypoglycemia. Reductions in plasma glucagon therefore predict defects in glycogenolysis in *PITP* $\alpha^{-/-}$ mice. Periodate acid-Schiff staining and visualization of glycogen rosettes by electron microscopy indicate substantial and inappropriate glycogen stores in *PITP* $\alpha^{-/-}$ liver (not shown). Quantitative analyses support these observations. As expected, *PITP* $\alpha^{+/+}$ liver contains $109.0 \pm 15.3 \mu\text{mol}$ of glycogen-derived glucose/g of tissue, and liver glycogen stores are depleted by a 10-h fast (Fig. 9C). Strikingly, the hypoglycemia of the mutant mice notwithstanding, *PITP* $\alpha^{-/-}$ liver contains $107.0 \pm 12.2 \mu\text{mol}$ of glycogen-derived glucose/g of tissue (Fig. 9C). This compares favorably to wild-type values.

To characterize further the derangement in glycogen metabolism, we tested whether glycogen stores in *PITP* $\alpha^{-/-}$ liver are resistant to depletion by fast. We found that a 10-h fast evokes

complete depletion of glycogen from mutant liver (Fig. 9C). When levels of liver glycogen are measured as a function of duration of fast in *PITP* $\alpha^{-/-}$ and *PITP* $\alpha^{+/+}$ animals, we found the rate of glycogen depletion from fasted *PITP* $\alpha^{-/-}$ liver is delayed. Whereas *PITP* $\alpha^{+/+}$ mice deplete ~50 and 70% of their liver glycogen stores by 2 and 4 h of fast, respectively, *PITP* $\alpha^{-/-}$ mice effect only a modest 23 and 27% depletion in liver glycogen stores after 2 and 4 h of fast, respectively (Fig. 9D). Taken together, these results are not consistent with an absolute block in *PITP* $\alpha^{-/-}$ liver glycogen catabolism. Rather, the data indicate *PITP* $\alpha^{-/-}$ liver exhibits kinetic defects in the rate of glycogenolysis and additionally suggest an inappropriate channeling of glucose to glycogen synthesis in the hypoglycemic mutant mouse.

Morphological Alterations in *PITP* $\alpha^{-/-}$ Pancreas—Reduced proglucagon gene expression could reflect specific derangement of proglucagon gene expression in the mutant animals or could arise indirectly from generalized pancreatic dysfunction. Although exocrine pancreas morphologies of *PITP* $\alpha^{+/+}$ and *PITP* $\alpha^{-/-}$ mice are similar, *PITP* $\alpha^{-/-}$ pancreas exhibits obvi-

TABLE III
Acyl chain compositions of bulk liver lipids

Fatty acid compositions of the lipid classes analyzed from pooled liver tissue samples depicted in Fig. 7 were analyzed. See the legend to Table II for essential details.

Acyl species	CE	TG	DAG	FFA	SM	CL
14:0	3.3/2.8	4.5/3.4	5.3/5.0	4.2/3.5	2.2/2.0	1.0/1.2
14:1n5	0.1/0.0	0.1/0.1	0.1/0.1	0.3/0.0	0.2/0.1	0.0/0.0
15:0	0.5/0.2	0.2/0.1	0.4/0.2	0.4/0.3	0.5/0.4	0.4/0.6
dm16:0	0.6/0.5	0.0/0.0	0.1/0.0	0.0/0.0	0.1/0.1	0.9/0.9
16:0	38.3/35.9	28.4/28.4	27.8/24.3	35.4/37.6	19.3/20.0	17.5/15.2
t16:1n7	1.0/0.5	0.4/0.5	1.0/0.8	1.4/1.2	1.0/0.5	0.6/0.6
16:1n7	5.3/5.8	2.1/1.8	1.6/1.6	1.7/1.2	1.7/1.4	0.7/0.9
dm18:0	0.0/0.1	0.1/0.1	0.0/0.0	0.1/0.1	0.0/0.0	0.3/0.3
dm18:1n9	0.8/0.0	0.0/0.0	0.0/0.0	0.0/0.0	0.0/0.1	0.1/0.1
dm18:1n7	0.1/0.4	0.0/0.0	0.0/0.0	0.0/0.0	0.0/0.0	0.1/0.1
18:0	9.5/5.8	4.1/3.3	9.0/6.2	9.4/10.5	22.5/22.3	15.9/14.5
t18:1n9	0.0/0.0	0.0/0.0	0.0/0.0	0.0/0.0	0.6/0.5	0.0/0.0
18:1n9	17.3/26.3	24.2/28.0	16.5/22.5	15.4/22.6	23.0/20.6	3.1/4.2
18:1n7	1.0/1.4	2.1/2.7	1.8/2.2	1.8/2.8	1.5/1.5	3.1/3.9
t18:2n6	0.1/0.0	0.0/0.0	0.0/0.0	0.0/0.0	0.1/0.2	0.0/0.0
18:2n6	11.5/11.8	21.8/23.4	18.9/23.2	15.8/12.1	5.0/4.5	29.5/36.9
18:3n6	0.3/0.3	0.4/0.4	0.4/0.5	0.2/0.1	0.1/0.1	0.1/0.1
18:3n3	0.7/0.6	0.6/0.4	0.8/0.7	0.5/0.1	0.5/0.4	0.5/0.4
18:4n3	0.0/0.0	0.1/0.1	0.0/0.1	0.0/0.0	0.0/0.0	0.0/0.0
20:0	0.2/0.1	0.1/0.0	0.3/0.2	0.2/0.2	0.3/0.5	0.1/0.2
20:1n15	0.0/0.0	0.0/0.0	0.0/0.0	0.0/0.0	0.0/0.0	0.0/0.0
20:1n12	0.0/0.0	0.0/0.0	0.0/0.0	0.0/0.0	0.0/0.0	0.0/0.0
20:1n9	0.3/0.2	0.6/0.5	0.2/0.4	0.3/0.6	0.4/0.3	0.1/0.3
20:3n9	0.0/0.0	0.2/0.2	0.3/0.3	0.2/0.4	0.0/0.0	0.0/0.1
20:2n6	0.4/0.2	0.7/0.6	0.7/0.6	0.9/1.0	0.2/0.2	6.6/3.6
20:3n6	0.8/0.6	1.0/0.7	1.0/1.0	1.2/0.7	0.8/0.9	0.6/0.6
20:4n6	3.2/2.7	2.4/1.5	4.5/3.7	7.3/4.0	9.8/11.2	5.6/5.2
20:3n3	0.0/0.0	0.0/0.0	0.1/0.1	0.1/0.0	0.1/0.1	0.1/0.1
20:4n3	0.2/0.0	0.1/0.0	0.1/0.1	0.1/0.0	0.0/0.0	0.1/0.1
20:5n3	0.4/0.3	0.3/0.2	0.4/0.3	0.5/0.1	0.4/0.4	0.3/0.2
22:0	0.3/0.3	0.0/0.0	0.1/0.0	0.0/0.0	0.6/0.4	0.1/0.1
22:1n9	1.3/0.9	0.2/0.1	0.0/0.1	0.1/0.2	0.4/0.2	0.6/0.4
22:2n6	0.0/0.0	0.1/0.0	0.0/0.2	0.1/0.1	0.0/0.0	0.0/0.0
22:4n6	0.0/0.0	0.0/0.0	0.0/0.0	0.0/0.0	0.0/0.0	0.0/0.0
22:5n6	0.0/0.0	0.0/0.0	0.0/0.0	0.0/0.0	0.0/0.0	0.0/0.0
22:5n3	0.2/0.1	1.0/0.4	1.0/0.7	0.0/0.4	0.7/0.7	0.3/0.3
22:6n3	1.8/1.5	4.1/1.7	7.6/5.1	1.6/0.2	6.4/7.2	11.4/8.7
24:0	0.6/0.5	0.1/0.1	0.0/0.0	0.3/0.1	0.3/0.6	0.1/0.1
24:1n9	0.1/0.0	0.0/1.0	0.0/0.0	0.0/0.0	1.3/2.6	0.1/0.1
24:6n3	0.0/0.0	0.2/0.2	0.0/0.0	0.0/0.0	0.0/0.0	0.0/0.0

ous structural defects in that pancreatic islets are not at all prominent. Serial sectioning of $PITP\alpha^{+/+}$ and $PITP\alpha^{-/-}$ pancreas, and quantification of total islets in the organ, revealed a greater than 2-fold reduction in absolute islet number in $PITP\alpha^{-/-}$ pancreas relative to wild type (Fig. 10A). In addition to the significant reduction in the number of islets, the morphology of identifiable islets in $PITP\alpha^{-/-}$ pancreas is also highly abnormal. Islet cells are sparse and shrunken, and large vacuolations are abundant in the islets themselves (Fig. 10B). The damage of pancreatic islets in $PITP\alpha^{-/-}$ mice provides a direct rationale for reduced proglucagon expression and defective gluconeogenesis in $PITP\alpha^{-/-}$ animals. Moreover, the very low levels of circulating insulin measured for $PITP\alpha^{-/-}$ mice (see above) may also result from islet β -cell insufficiencies and not simply from the hypoglycemic state of these animals.

$PITP\alpha^{-/-}$ Cells Are Not Generally Defective in UPR—A linkage between activation of UPR and survival of pancreatic secretory islet cells has been demonstrated (34, 35). The ER abnormalities in $PITP\alpha$ -deficient enterocytes, hepatocytes, and neurons, when coupled with loss of functional pancreatic islets in mutant mice, suggested the possibility that $PITP\alpha^{-/-}$ cells are intrinsically defective in UPR.

First, we compared the response of $PITP\alpha^{+/+}$ and $PITP\alpha^{-/-}$

ES cells and MEFs to glucose deprivation. Cells defective in UPR are sensitive to such a challenge (34). In neither case do we record an unusual sensitivity of $PITP\alpha^{-/-}$ cells to glucose deprivation. $PITP\alpha^{+/+}$ ES cells maintain levels of viability that are 71 ± 5 and $55 \pm 8\%$ of control after 42 and 72 h of glucose starvation, respectively. The corresponding viability levels for isogenic $PITP\alpha^{-/-}$ ES cells are 71 ± 4 and $54 \pm 10\%$ (Fig. 10C). Similarly, $PITP\alpha^{+/+}$ MEFs exhibit viabilities of 82 ± 5 and $73 \pm 10\%$ after glucose deprivations of 42 and 72 h, respectively. Isogenic $PITP\alpha^{-/-}$ MEFs exhibit corresponding viabilities of 84 ± 4 and $76 \pm 8\%$ (Fig. 10C).

Second, ^{35}S -labeled amino acid pulse-radiolabeling experiments demonstrate that treatment of $PITP\alpha^{+/+}$ and isogenic $PITP\alpha^{-/-}$ ES cells with agents that activate UPR (*i.e.* dithiothreitol) evoke reduced incorporation of ^{35}S -labeled amino acids into nascent protein in both wild-type and mutant ES cells. The rate of protein synthesis in the face of dithiothreitol is 7.2 ± 0.7 and $5.2 \pm 0.7\%$ of unchallenged control for $PITP\alpha^{+/+}$ and $PITP\alpha^{-/-}$ ES cells, respectively (Fig. 10D). This effect is a result of a UPR-mediated translational block (34). These findings are qualitatively reproduced in other experiments that employed thapsigargin challenge to induce UPR (Fig. 10D).

Finally, we assessed whether challenge of $PITP\alpha^{+/+}$ and

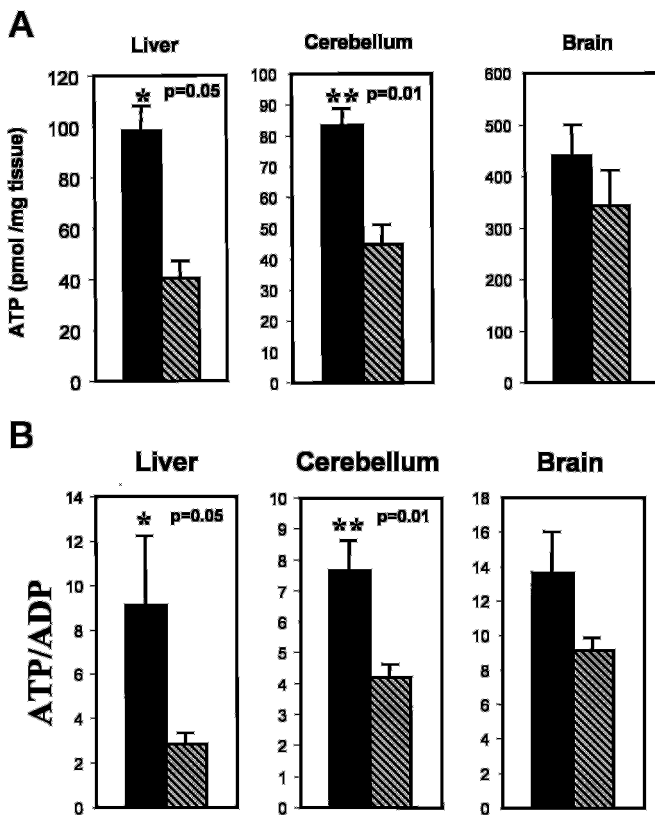


FIG. 8. Tissue-specific energy deficits in *PITP* $\alpha^{-/-}$ mice. A, tissue ATP levels in *PITP* $\alpha^{-/-}$ mice. Measurements were averaged for three determinations from each of three independent P4-P6 *PITP* $\alpha^{+/+}$ (solid bars) and *PITP* $\alpha^{-/-}$ animals (hatched bars). B, ATP/ADP ratios for the indicated tissues. ADP was measured indirectly by conversion to ATP and measurement of ADP-derived ATP. No significant differences in ATP or ATP/ADP ratio were observed between measurements of cerebellar hemispheres, or selected brain or liver regions, and those of whole-organ homogenates. *PITP* $\alpha^{+/+}$ and *PITP* $\alpha^{-/-}$ data are in solid and hatched bars, respectively.

PITP $\alpha^{-/-}$ MEFs and ES cells with the UPR-activating agent tunicamycin leads to a differential response in expression of the ER stress-induced transcription factor CHOP and the chaperone protein calnexin. Expression of these two polypeptides is potently enhanced by induction of the UPR. Thus, CHOP and calnexin serve as reliable reporters of the UPR status in cells. As shown in Fig. 10E, CHOP is normally expressed at very low levels in *PITP* $\alpha^{+/+}$ and *PITP* $\alpha^{-/-}$ MEFs, but challenge with tunicamycin evokes a robust induction of CHOP expression in MEFs of either genotype. Similarly, calnexin levels increase in both *PITP* $\alpha^{+/+}$ and *PITP* $\alpha^{-/-}$ MEFs upon tunicamycin challenge (Fig. 10E). Congruent results are recorded with *PITP* $\alpha^{+/+}$ and *PITP* $\alpha^{-/-}$ ES cells (not shown). We conclude *PITP* $\alpha^{-/-}$ cells are not only competent for induction of UPR but that the nullizygous cells are not subject to constitutive activation of the UPR.

DISCUSSION

Loss of *PITP* α activity in mice manifests itself in spinocerebellar disease characterized by reactive gliosis of the cerebellum and brain stem and WM and GM deficits in spinal cord. The spinal cord pathologies include infiltration by inflammatory cells, aponecrosis of motor neuron cell bodies in the ventral horn, and pervasive demyelination that is particularly apparent in the dorsal columns. *PITP* α is also required for proper absorption of dietary fat and fat-soluble vitamins through duodenal enterocytes into the circulation and for proper lipid

homeostasis in the liver. Finally, *PITP* $\alpha^{-/-}$ mice are severely hypoglycemic. The hypoglycemia is associated with reduced proglucagon gene expression, compromise of pancreatic islet integrity, and defects in liver glycogen metabolism. These findings suggest unanticipated roles for *PITP* α in signaling pathways that interface with trafficking of luminal lipid cargo from the ER and glucose homeostasis in mammals.

PITP α and Neonatal Survival—The development of *PITP* $\alpha^{-/-}$ mice to term supports our finding that *PITP* α -deficient ES cells maintain pluripotency and competence for membrane trafficking and growth factor signaling (17). Rather, the neonatal mortality of *PITP* $\alpha^{-/-}$ mice indicates a role for *PITP* α in regulating physiological functions that are critical in the context of the whole mouse. We conclude *PITP* α nullizygosity manifests itself primarily upon extinction (by birth) of the nutritional resource provided by maternal circulation *in utero*, and reliance of the neonate on assimilation of its own dietary intake.

PITP α Deficiency and Steatosis—The most energy-rich component of the neonatal diet is TG, and the evidence suggests *PITP* $\alpha^{-/-}$ mice are unable to effectively avail themselves of this nutrient source. In mammals, long chain TGs of maternal milk are hydrolyzed to monoacylglycerols and fatty acids. These compounds are transported across the apical enterocyte plasma membrane and reassembled into TG cores in the smooth ER lumen. The TG cores are then co-assembled with other lipids, fat-soluble vitamins, and apolipoproteins into chylomicrons either in the ER or in the Golgi complex. Subsequently, chylomicrons are transported across the enterocyte basolateral plasma membrane via the secretory pathway (37). Enterocytes and hepatocytes share analogous pathways for assembly and secretion of lipoproteins into the circulation. The suckling-dependent microvesicular steatosis of *PITP* $\alpha^{-/-}$ intestine and liver suggests that *PITP* α plays a common role in both intestinal and hepatic pathways for secretion of dietary lipids. A failure in transport early in the secretory pathway is indicated as electron microscopy suggests neutral lipids accumulate in smooth ER of *PITP* α nullizygous enterocytes and in hepatocytes.

The intestinal steatosis of *PITP* $\alpha^{-/-}$ mice exhibits similarities with human CRD, a family of autosomal recessive disorders. Human CRD patients are characterized by pediatric failure to thrive, accumulation of chylomicrons within villus-associated enterocytes of the duodenum, reductions in post-prandial plasma TG and α -tocopherol levels, and spinocerebellar involvement (18, 19, 32, 38). Similarly, *PITP* $\alpha^{-/-}$ mice gain body mass slowly and are deficient in body fat. Moreover, villus-associated *PITP* $\alpha^{-/-}$ enterocytes accumulate intracellular lipid in a suckling-dependent manner. Finally, *PITP* $\alpha^{-/-}$ mice exhibit large reductions in both post-prandial plasma TG and in brain α -tocopherol. These data suggest *PITP* $\alpha^{-/-}$ mice hydrolyze dietary TG in the lumen of the duodenum, transport the products into the enterocyte, and properly reassemble dietary TG in the ER lumen but are defective in transport of re-esterified TGs across the *PITP* $\alpha^{-/-}$ enterocyte to the basolateral plasma membrane. The microvesicular hepatic steatosis we observe in *PITP* $\alpha^{-/-}$ mice is not a symptom associated with human CRD, however.

PITP α Deficiency and Glucose Homeostasis—*PITP* $\alpha^{-/-}$ neonates are hypoglycemic, even though key gluconeogenic enzymes appear to be expressed normally. However, gluconeogenesis is an energetically expensive process as 4ATP, 2GTP, 2NADH, and 4H₂O are consumed in conversion of 2 pyruvate units to 1 glucose molecule (39). Fatty acid oxidation is a potent engine that drives production of the ATP, GTP, and NADH utilized in glucose synthesis and is also involved in production

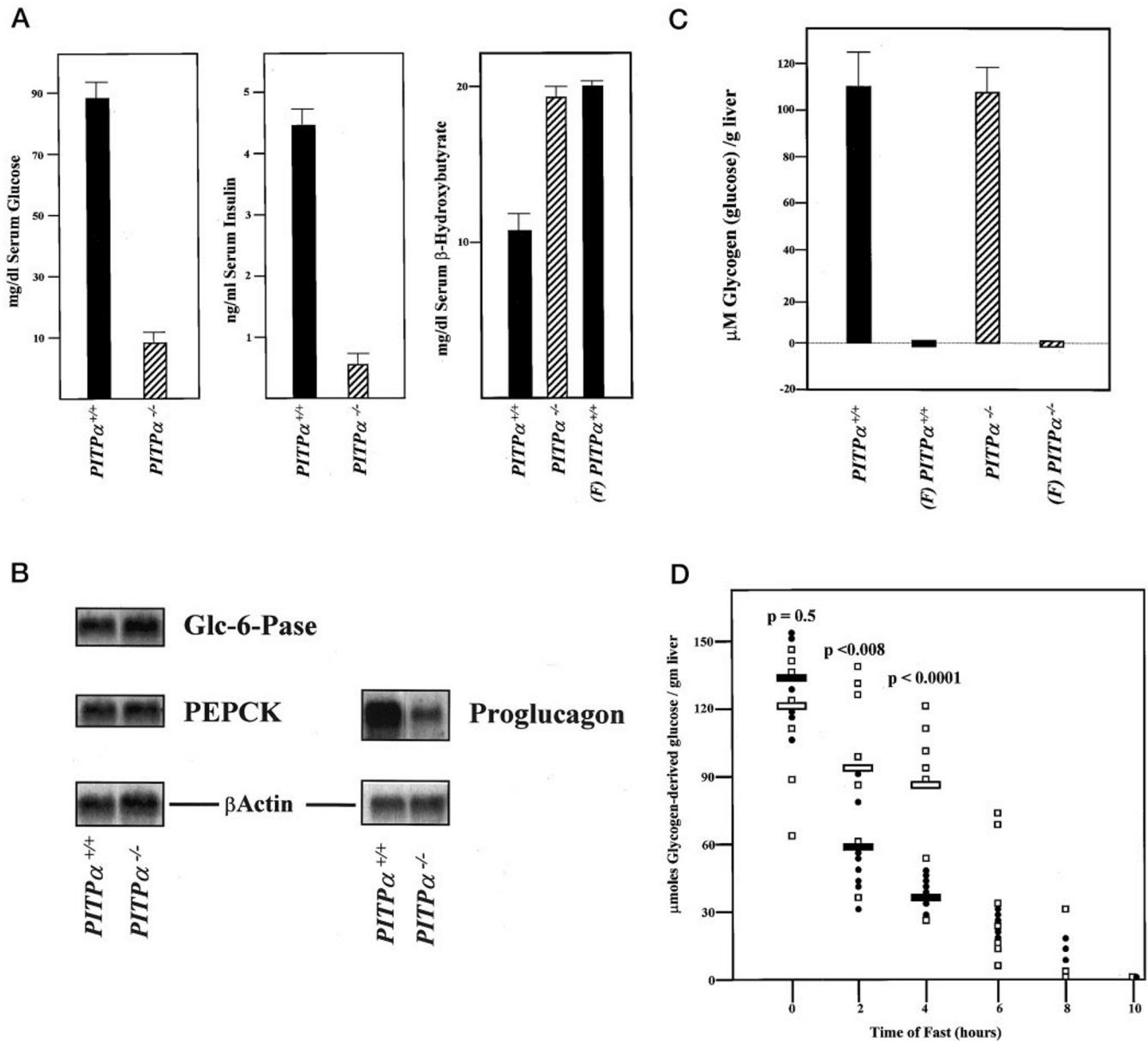


FIG. 9. Hypoglycemia in $PITP\alpha^{-/-}$ mice. A, serum glucose, insulin, and β -hydroxybutyrate levels. Serum was collected from age-matched $PITP\alpha^{+/+}$ (closed bars) and $PITP\alpha^{-/-}$ (hatched bars) mice. Glucose data are averaged from six age-matched $PITP\alpha^{+/+}$ and $PITP\alpha^{-/-}$ mice of each genotype. Serum insulin and β -hydroxybutyrate values represent averages of triplicate measurements obtained from three mice of each genotype. Values from fasted $PITP\alpha^{+/+}$ mice (18 h) are indicated by F. B, Glc-6-Pase, phosphoenolpyruvate carboxykinase (PEPCK), and β -actin mRNA levels in $PITP\alpha^{+/+}$ and $PITP\alpha^{-/-}$ liver, and proglucagon and β -actin mRNA levels in pancreas. Data are representative of at least three independent mRNA extractions and hybridizations. RNA load was normalized to 10 μ g total mRNA per lane, and the β -actin data serve as indicators of normalization quality. C, glycogen was quantified for non-fasted and fasted $PITP\alpha^{+/+}$ and $PITP\alpha^{-/-}$ liver, as indicated. D, kinetics of liver glycogen depletion. Age-matched $PITP\alpha^{+/+}$ (\bullet) and $PITP\alpha^{-/-}$ (\square) mice with stomachs full of milk were fasted as indicated, sacrificed, and liver glycogen measured. Mean glycogen values are given for $PITP\alpha^{+/+}$ and $PITP\alpha^{-/-}$ liver as solid and open bars, respectively, and statistical significance of the mean differences is given above each data set.

of ketone bodies that serve as energy sources under conditions of low glucose availability. We suggest that the inability to effectively deliver lipid from enterocytes and hepatocytes to peripheral tissues imposes a heavy metabolic burden on $PITP\alpha^{-/-}$ neonates by compromising fatty acid oxidation as a pathway for powering both gluconeogenesis and ketone production. Reductions in $PITP\alpha^{-/-}$ liver ATP are consistent with this interpretation of the data.

In addition, $PITP\alpha^{-/-}$ animals exhibit kinetic defects in glycogenolysis, and these maintain substantial liver glycogen in the face of hypoglycemia. These defects coincide with dramatic reductions in proglucagon gene expression in $PITP\alpha^{-/-}$ pancreas. Presently, we do not believe that dysregulation of proglucagon expression reflects a direct transcriptional in-

volvement of a nuclear $PITP\alpha$ pool in regulating proglucagon promoter function. Rather, we hypothesize that glucagon deficit in $PITP\alpha^{-/-}$ mice more likely represents an indirect manifestation of the structurally compromised endocrine pancreas that characterizes such mutants. Yet, because the glycogen stores of $PITP\alpha^{-/-}$ liver are consumed during a modest fast, we conclude that regulation of glucose allocation into the glycogen synthesis pathway must also be deranged in $PITP\alpha^{-/-}$ mice.

$PITP\alpha$ Deficiency and Integrity of the Spinocerebellar System— $PITP\alpha^{-/-}$ neonates develop a spinocerebellar neurodegenerative disease characterized by apoptotic cell death. In this regard, we find a correlation between site of neuronal injury and regional specificity of dramatic reduction in cellular

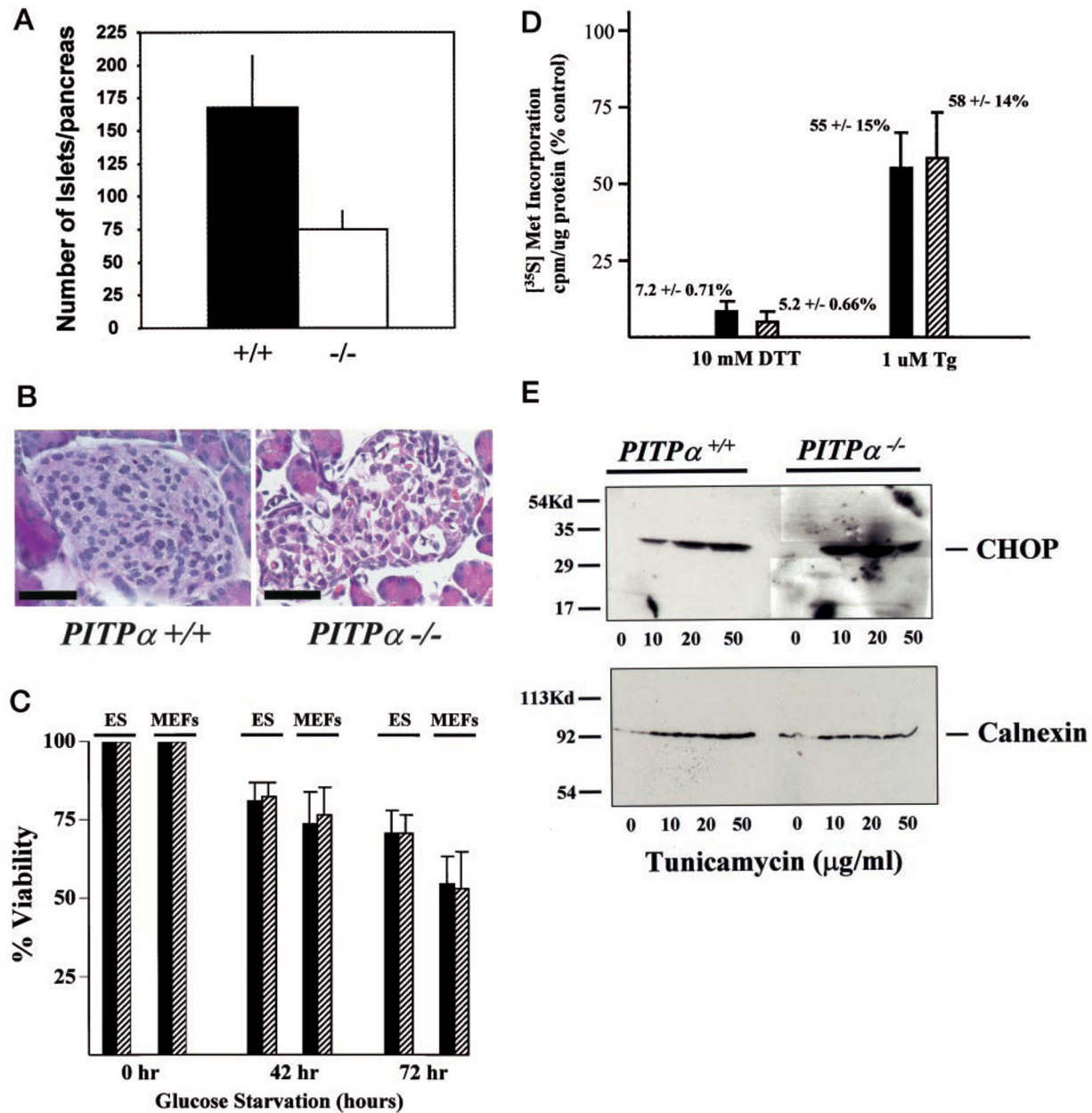


FIG. 10. Pancreatic islet cells and the unfolded protein response in *PITP* α ^{-/-} mice. *A*, number of pancreatic islets in whole pancreas from *PITP* α ^{+/+} and *PITP* α ^{-/-} mice. Whole pancreata were recovered from each of two *PITP* α ^{+/+} and *PITP* α ^{-/-} mice. The individual *PITP* α ^{+/+} pancreata were serially sectioned into 48 and 60 consecutive sections, respectively, whereas both *PITP* α ^{-/-} pancreata were each sectioned into 48 serial sections. Islets were then comprehensively counted for every section of each individual pancreas so that the total number of islets per organ was determined. The data represent the averages of the two reconstructions for *PITP* α ^{+/+} and *PITP* α ^{-/-} pancreas (solid and open bars, respectively). *B*, histology of endocrine pancreas. Images from hematoxylin/eosin-stained sections of *PITP* α ^{+/+} and *PITP* α ^{-/-} pancreas. Bars are 50 μ m. *C*, viability of *PITP* α ^{+/+} (solid bars) and *PITP* α ^{-/-} (hatched bars) ES cells and MEFs as a function of period of glucose starvation is indicated. Living cells were identified by a trypan blue exclusion assay. *D*, ER stress-induced inhibition of protein synthesis. MEFs of appropriate genotype (*PITP* α ^{+/+}, solid bars; *PITP* α ^{-/-}, hatched bars) were incubated in the presence or absence of 10 mM dithiothreitol (DTT; 15 min) or 1 μ M thapsigargin (Tg; 30 min) prior to and during a 20-min pulse-radiolabeling with [³⁵S]methionine (100 μ Ci/ml). Relative incorporation of radiolabel into protein was quantified as trichloroacetic acid-precipitable radioactivity and is presented as an average percentage of that measured for mock-treated control cells (100%). Values are derived from triplicate determinations from three independent experiments. *PITP* α ^{+/+} and *PITP* α ^{-/-} MEFs exhibit essentially indistinguishable rates of incorporation of [³⁵S]methionine into protein. *E*, CHOP and calnexin expression. Cell-free extracts were prepared from *PITP* α ^{+/+} and *PITP* α ^{-/-} MEFs after an 18-h incubation with 0, 10, 20, and 50 μ g/ml tunicamycin (at bottom). Equivalent amounts of protein were loaded for each sample (20 μ g) and resolved by SDS-PAGE. Proteins were transferred to nitrocellulose, and the resulting blot was probed with anti-CHOP and anti-calnexin antibodies (Santa Cruz Biotechnology) and developed by enhanced chemiluminescence.

ATP. Neonatal cerebellum may be particularly sensitive to injury in *PITP* α ^{-/-} mice because it attempts to sustain the extraordinary rates of cell proliferation that accompany the postnatal development of this organ in the face of a challenging energetic environment. Similarly, Purkinje cells and motor neurons are very large and metabolically active cells that are sensitive to a variety of insults. We suggest *PITP* α ^{-/-} Purkinje

cell and motor neuron defects also represent manifestations of energy deficit in these cells, thereby raising the possibility that a significant component of the spinocerebellar disorder arises from the intrinsic hypoglycemia and/or the intestinal and hepatic steatosis of *PITP* α ^{-/-} mice.

Cellular Mechanisms for PITP α Function in the Mouse?—The lines of evidence linking PITP α to potentiation of PIP

synthesis suggest that the tissue defects of *PITP α ^{-/-}* mice result from deranged PIP metabolism. A demonstration that this is indeed the case remains elusive as such derangements are not apparent in bulk PtdIns, PtdIns-3-phosphate, PtdIns-4-phosphate, or PtdIns-4,5-bisphosphate levels in *PITP α ^{-/-}* ES cells (17) or MEFs (this study, not shown). Our data indicate that *PITP α* does not play a critical role in regulating dynamics of cell-essential phospholipid pools in most cell types.

With regard to dysregulation of cellular homeostasis in *PITP α* nullizygous mice, we find that derangement of ER function is a common theme. *PITP*s are classically invoked to function as lipid carriers that ferry PtdIns from its ER site of synthesis to signaling membranes (plasma membrane and Golgi) so that dynamic PIP pools can be replenished. In its simplest form, this model predicts that *PITP α* deficiency will compromise signaling in membranes distinct from the ER. Although it remains possible that disruptions of *PITP α* -mediated signaling in non-ER compartments manifest themselves indirectly in an ER pathology, the consistent smooth ER abnormalities of *PITP α ^{-/-}* spinal and cerebellar neurons, enterocytes, and hepatocytes suggest that the ER may itself represent a primary target of *PITP α* function. In this regard, *PITP α* -dependent egress of PtdIns from the cytoplasmic leaflet of ER membranes may be required for ER function via unanticipated mechanisms. Alternatively, *PITP α* may play unforeseen ER signaling functions that do not require *PITP α* -mediated transfer of lipid between organelles.

With regard to ER functions for *PITP α* , we entertained the idea that coupling of induction of UPR to ER secretory load is *PITP α* -dependent and is compromised in *PITP α ^{-/-}* cells. Although our finding that *PITP α ^{-/-}* ES cells and MEFs are UPR-competent argues against this idea, we cannot exclude the possibility that UPR defects in *PITP α ^{-/-}* mice are manifested only in professional secretory tissues (e.g. pancreatic islet cells, Purkinje cells, enterocytes, and hepatocytes) where high levels of cargo processing in the ER must occur efficiently.

An alternative possibility is that *PITP α* plays a direct and specific role in membrane trafficking from the ER in professional secretory cells by playing a direct role in facilitating membrane trafficking at the level of budding of specific ER-derived transport vesicles. This proposed activity is congruent with the role of *PITP*s in yeast membrane trafficking (1, 3–5). The accumulation of dietary neutral lipids in the lumen of the enterocyte and hepatocyte ER is consistent with such a function. Although constitutive and regulated secretory pathway function is normal in *PITP α ^{-/-}* ES cells (17), and development of *PITP α ^{-/-}* mice to term is also inconsistent with wholesale defects in membrane trafficking from the ER of nullizygous cells, we propose that the ER membrane trafficking function of *PITP α* exhibits a large degree of cargo specificity.

Is there independent supporting evidence for such a proposal? It was recently demonstrated that inactivation of the *SARA2* isoform of the Sar1p GTPase forms a genetic basis for human CRD (40). Sar1p is required for the budding of COPII vesicles from ER membranes and for the concentration of cargo into such transport vesicles (41). Our data, when coupled with the demonstrations of a role for Sar1p in human CRD, suggest the attractive hypothesis that *PITP α* regulates the Sar1p GTPase cycle in ER membranes. We propose that a dedicated *PITP α /Sar1p* interface is required to optimize assembly and packaging of unusual luminal cargoes (such as large TG cores) into ER-derived transport vesicles. This model shares common features with previous proposals positing that the Sec14p *PITP* regulates the activity of specific ADP-ribosylation factor

GTPase-activating proteins required for biogenesis of secretory cargo-laden transport vesicles from *trans*-Golgi membranes in yeast (6, 42).

Acknowledgments—We acknowledge Douglas Cyr, Andrew Morris, Patrick Brennwald, Peter Petrusz, John York, Tushar Patel, William Snider, Virginia Godfrey, Scott Traske, and Rosalind Coleman for helpful discussions. We are particularly grateful to Gail Grossman for expert assistance in histochemistry; Hal Mekeel for helpful advice on electron microscopy; Patricia Gallagher for expert assistance in α -tocopherol measurements (University of North Carolina Clinical Nutrition Research Center supported by National Institutes of Health Grant DK56350); David Brenner and Joe Grisham for expert advice on liver histopathology; Lisa M. Bain for brain histology; and Heather Collins and Bryan Wolf (University of Pennsylvania Diabetes Center) for glucagon and corticosteroid measurements. Support for body composition assays were provided by grants from the National Institutes of Health to the University of Alabama at Birmingham Clinical Nutrition Research Center.

REFERENCES

- Cleves, A. E., McGee, T. P., and Bankaitis, V. A. (1991) *Trends Cell Biol.* **1**, 30–34
- Wirtz, K. W. A. (1991) *Annu. Rev. Biochem.* **60**, 73–99
- Bankaitis, V. A., Aitken, J. R., Cleves, A. E., and Dowhan, W. (1990) *Nature* **347**, 561–562
- Cleves, A. E., McGee, T. P., Whitters, E. A., Champion, K. M., Aitken, J. R., Dowhan, W., Goebel, M., and Bankaitis, V. A. (1991) *Cell* **64**, 789–800
- Kearns, B. G., Alb, J. G., Jr., and Bankaitis, V. A. (1998) *Trends Cell Biol.* **8**, 276–282
- Yanagisawa, L., Marchena, J., Xie, Z., Li, X., Poon, P. P., Singer, R., Johnston, G., Randazzo, P. A., and Bankaitis, V. A. (2002) *Mol. Biol. Cell* **13**, 2193–2206
- Sha, B., Phillips, S. E., Bankaitis, V. A., and Luo, M. (1998) *Nature* **391**, 506–510
- Yoder, M. D., Thomas, L. M., Tremblay, J. M., Oliver, R. L., Yarbrough, L. R., and Helmkamp, G. M., Jr. (2001) *J. Biol. Chem.* **276**, 9246–9252
- Dickeson, S. K., Lim, C. N., Schuyler, G. T., Dalton, T. P., Helmkamp, G. M., Jr., and Yarbrough, L. R. (1989) *J. Biol. Chem.* **264**, 16557–16564
- Tanaka, S., and Hosaka, K. (1994) *J. Biochem. (Tokyo)* **115**, 981–984
- Fullwood, Y., dos Santos, M., and Hsuan, J. J. (1999) *J. Biol. Chem.* **274**, 31553–31558
- Hay, J. C., and Martin, T. F. J. (1993) *Nature* **366**, 572–575
- Ohashi, M., de Vries, K. J., Frank, R., Snoek, G., Bankaitis, V., Wirtz, K., and Huttner, W. B. (1995) *Nature* **377**, 544–547
- Cunningham, E., Tan, S. K., Swigart, P., Hsuan, J., Bankaitis, V. A., and Cockcroft, S. (1996) *Proc. Natl. Acad. Sci. U. S. A.* **93**, 6589–6593
- Milligan, S. C., Alb, J. G., Jr., Elagina, R. B., Bankaitis, V. A., and Hyde, D. R. (1997) *J. Cell Biol.* **139**, 351–363
- Hamilton, B. A., Smith, D. J., Mueller, K. L., Kerrebrock, A. W., Bronson, R. T., van Berkel, V., Daly, M. J., Kruglyak, L., Reeve, M. P., Nemhauser, J. L., Hawkins, T. L., Rubin, E. M., and Lander, E. S. (1997) *Neuron* **18**, 711–722
- Alb, J. G., Jr., Phillips, S. E., Rostand, K., Cotlin, L., Pinxteren, J., Manning, T., Guo, S., York, J. D., Sontheimer, H., Collawn, J. F., and Bankaitis, V. A. (2002) *Mol. Biol. Cell* **13**, 739–754
- Levy, E. (1996) *Clin. Invest. Med.* **19**, 317–324
- Aguglia, U., Annesi, G., Pasquinelli, G., Spadafora, P., Gambarella, A., Annesi, F., Pasqua, A. A., Cavalcanti, F., Crescibene, L., Bagala, A., Bono, F., Oliveri, R. L., Valentino, P., Zappia, M., and Quattrone, A. (2000) *Ann. Neurol.* **47**, 260–264
- Zambrowicz, B. P., Friedrich, G. A., Buxton, E. C., Lilleberg, S. L., Person, C., and Sands, A. T. (1998) *Nature* **392**, 608–611
- Nagy, T. R., Gower, B. A., and Stetson, M. H. (1994) *Can. J. Zool.* **72**, 1726–1734
- Luna, L. (1968) *Manual of Histological Staining Methods of the Armed Forces Institute of Pathology*, pp. 143–145, Armed Forces Institute of Pathology, Washington, DC
- Mascorro, J. A., and Kirby, G. S. (1986) *Proceedings of the 44th Annual Meeting of the Electron Microscopy Society of America*, pp. 222–223
- Sato, T. (1968) *J. Electron Microscop.* **17**, 158–159
- Jishage, K., Arita, M., Igarashi, K., Iwata, T., Watanabe, M., Ogawa, M., Ueda, O., Kamada, N., Inoue, K., Arai, H., and Suzuki, H. (2001) *J. Biol. Chem.* **276**, 1669–1672
- Passonneau, J., and Lauderdale, V. (1974) *Anal. Biochem.* **60**, 405–412
- Formigli, L., Papucci, L., Tani, A., Schiavone, N., Tempestini, A., Orlandini, G. E., Capaccioli, S., and Zecchi Orlandini, S. (2000) *J. Cell. Physiol.* **182**, 41–49
- Sperandio, S., de Belle, I., and Bredesen, D. E. (2000) *Proc. Natl. Acad. Sci. U. S. A.* **97**, 14376–14381
- Galli, S. J., Dvorak, A. M., and Dvorak, H. F. (1984) *Prog. Allergy* **34**, 1–141
- Bebo, B. F., Jr., Yong, T., Orr, E. L., and Linthicum, D. S. (1996) *J. Neurosci. Res.* **45**, 340–348
- Pender, M. P., Stanley, G. P., Yoong, G., and Nguyen, K. B. (1990) *Acta Neuropathol.* **80**, 172–183
- Roy, C. C., Levy, E., Green, P. H. R., Sniderman, A., Letarte, J., Buts, J.-P., Orquin, J., Brochu, P., Weber, A. M., Morin, C. L., Marcel, Y., and Deckelbaum, R. J. (1987) *Gastroenterology* **92**, 390–399
- Hanson, R. W., and Reshef, L. (1997) *Annu. Rev. Biochem.* **66**, 581–611
- Harding, H. P., Zeng, H., Zhang, Y., Jungries, R., Chung, P., Plesken, H., Sabatini, D. D., and Ron, D. (1983) *Mol. Cell* **7**, 1153–1163

35. Scheuner, D., Song, B., McEwen, E., Liu, C., Laybutt, R., Gillespie, P., Saunders, T., Bonner-Weir, S., and Kaufman, R. J. (2001) *Mol. Cell* **7**, 1165–1176
36. Weimar, W. R., Lane, P. W., and Sidman, R. L. (1982) *Brain Res.* **251**, 357–364
37. Hussain, M. M., Kanch, R. K., Zhou, Z., Luchmoon, J., Zu, H., and Bakillah, A. (1996) *Biochim. Biophys. Acta* **1300**, 151–170
38. Gauthier, S., and Sniderman, A. (1983) *Ann. Neurol.* **14**, 591
39. Nelson, D. L., and Cox, M. M. (2000) *Lehninger Principles of Biochemistry*, 3rd Ed., p. 729, Worth Publishers, New York
40. Jones, B., Jones, E. L., Bonney, S. A., et al. (2003) *Nat. Genet.* **34**, 29–31
41. Schekman, R., and Orci, L. (1996) *Science* **271**, 1526–1533
42. Li, X., Rivas, M. P., Fang, M., Marchena, J., Mehrotra, B., Chaudhary, A., Feng, L., Prestwich, G. D., and Bankaitis, V. A. (2002) *J. Cell Biol.* **157**, 63–77